

This is an Accepted Manuscript for *Journal of Glaciology*. Subject to change during the editing and production process.
DOI: 10.1017/jog.2024.49

Vulnerability of firn to hydrofracture: poromechanics modeling

Yue Meng,^{1,3} Riley Culberg,^{2,3} Ching-Yao Lai^{1,3}

¹*Department of Geophysics, Stanford University, Stanford, CA, USA*

²*Department of Earth and Atmospheric Sciences, Cornell University, Ithaca, NY, USA*

³*Department of Geosciences, Princeton University, Princeton, NJ, USA*

Correspondence: Yue Meng <olivmeng@stanford.edu>, Riley Culberg <rtc84@cornell.edu>

ABSTRACT. On the Greenland Ice Sheet, hydrofracture connects the supraglacial and subglacial hydrologic systems, coupling surface runoff dynamics and ice velocity. In recent decades, the growth of low-permeability ice slabs in the wet snow zone has expanded Greenland's runoff zone, but observations suggest that surface-to-bed connections are rare, because meltwater drains through crevasses into the porous firn beneath ice slabs. However, there is little quantitative evidence confirming the absence of surface-to-bed fracture propagation. Here, we use poromechanics to investigate whether water-filled crevasses in ice slabs can propagate vertically through an underlying porous firn layer. Based on numerical simulations, we develop an analytical estimate of the water injection-induced effective stress in the firn given the water level in the crevasse, ice slab thickness, and firn properties. We find that the firn layer substantially reduces the system's vulnerability to hydrofracture because much of the hydrostatic stress is accommodated by a change in pore pressure, rather than being transmitted to the solid skeleton. This result suggests that surface-to-bed hydrofracture will not occur in ice slab regions until all pore space proximal to the initial flaw has been filled with solid ice.

This is an Open Access article, distributed under the terms of the Creative Commons Attribution-NonCommercial-NoDerivatives licence (<http://creativecommons.org/licenses/by-nc-nd/4.0/>), which permits non-commercial re-use, distribution, and reproduction in any medium, provided the original work is unaltered and is properly cited. The written permission of Cambridge University Press must be obtained for commercial re-use or in order to create a derivative work.

1. INTRODUCTION

Over the last two decades, around 55% of mass loss from the Greenland Ice Sheet has come from the runoff of surface meltwater, with the remainder driven by ice dynamics (Mouginot and others, 2019; Van Den Broeke and others, 2009). Passive microwave observations and regional climate models also show a long-term increase in the area of the ice sheet experiencing surface melt, the maximum elevation of where melting occurs, and the total length of the annual melt season (Colosio and others, 2021; Fettweis and others, 2011). Therefore, understanding how much and how quickly surface meltwater can be transported through the supraglacial and englacial hydrologic systems and how those systems are evolving with time is critical for assessing current and future sea level contributions from the Greenland Ice Sheet.

Water transport processes vary significantly across the ice sheet. In the bare ice ablation zone, surface meltwater flows efficiently over the impermeable ice surface in streams or rivers and forms lakes in closed basins (Smith and others, 2015; Yang and Smith, 2016). Particularly in Southwest Greenland, this supraglacial system is connected to the ice sheet bed through fractures, moulins, and rapid lake drainage events, and most melt eventually enters the subglacial system (Das and others, 2008; Koziol and others, 2017; Poinar and Andrews, 2021; Andrews and others, 2018; Hoffman and others, 2018; Dow and others, 2015; Lai and others, 2021). These englacial transport pathways are primarily formed by hydrofracture (Stevens and others, 2015; Poinar and others, 2017) and lead to a coupling between surface melting and ice dynamics, where meltwater delivery to the bed can cause transient, seasonal increases in ice velocity that may temporarily increase ice discharge (Moon and others, 2014; Schoof, 2010; Zwally and others, 2002).

In contrast, in the accumulation zone, meltwater percolates in the porous near-surface firn layer, where it may refreeze locally (Harper and others, 2012; Machguth and others, 2016) or be stored in buried liquid water aquifers (Forster and others, 2014). These processes buffer runoff and prevent water from reaching the subglacial system as long as pore space remains for storage. The processes by which the percolation zone may transition to a bare ice ablation zone under persistent atmospheric warming are not yet fully understood, particularly the timescales over which the hydrologic system evolves from local retention to efficient runoff and drainage.

The development of multi-meter thick ice slabs in the near-surface firn of the wet snow zone appears to be one mechanism by which the ice sheet may transition rapidly from retention to runoff. These continuous, low-permeability layers of refrozen ice block vertical percolation and allow water to flow freely over the

54 surface, despite the presence of a relict porous firn layer at depth (MacFerrin and others, 2019; Tedstone
55 and Machguth, 2022). This produces a surface hydrologic network that qualitatively resembles that of the
56 bare ice ablation zone (Tedstone and Machguth, 2022; Yang and Smith, 2016). However, similar to the data
57 shown in Figure 1, Culberg and others (2022) presented observational evidence from Northwest Greenland
58 that when surface meltwater drains into surface crevasses in ice slabs, it is stored in the underlying relict
59 firn layer where it refreezes into “ice blobs” and does not reach the ice sheet bed. Therefore, they suggest
60 that meltwater in ice slab regions is unlikely to influence the subglacial system, and that surface-to-bed
61 connections may not develop until all local firn pore space is depleted (Culberg and others, 2022).

62 While Culberg and others (2022) present strong evidence for large-scale water storage in ice blobs, their
63 evidence that fractures do not propagate through the firn layer and that no water drains deeper into the
64 englacial system is at best circumstantial. The ice-penetrating radar data they present do not directly
65 resolve any surface crevasses (see Figure 1 for example) and the ice blobs were imaged anywhere from 6
66 months to 5 years after the initial drainage (Culberg and others, 2022), by which time any deep englacial
67 pathways would have closed by creep. The authors speculated that leak-off into the permeable firn might
68 reduce the crack tip stress enough to prevent unstable propagation, based on literature from the hydraulic
69 fracking community (Culberg and others, 2022). However, to date there have been no investigations of
70 hydrofracture processes in firn, leaving no direct quantitative support for this assumption. In principle, it
71 is possible that ice blobs represent leak-off from the walls of much deeper crevasses that were at one time
72 fully filled with water. Even if ice blobs only form when fractures cannot propagate through the firn, there
73 is currently no way to investigate whether these drainage dynamics are particular to Northwest Greenland,
74 or if this response should generalize to the entire Greenland ice sheet or potentially even to Antarctic ice
75 shelves.

76 Current models of ice sheet hydrofracture are not suited to investigating this question. The most
77 common approach is to use linear elastic fracture mechanics (LEFM). For example, Lai and others (2020)
78 treated the effects of a near-surface firn layer on dry fracture propagation on Antarctic ice shelves. They
79 assumed that due to its lower density, the presence of firn leads to a lower overburden stress and reduced
80 viscosity. However, their analysis for firn focuses only on water-free crevasse. For analysis of hydrofracture
81 in firn, leakage of water into the firn needs to be considered, whereas LEFM analyses typically assume that
82 the medium is impermeable and incompressible. In fact, work in other fields on the hydraulic fracturing of
83 permeable reservoir suggests that it is the compressibility and permeability of the medium that can lead

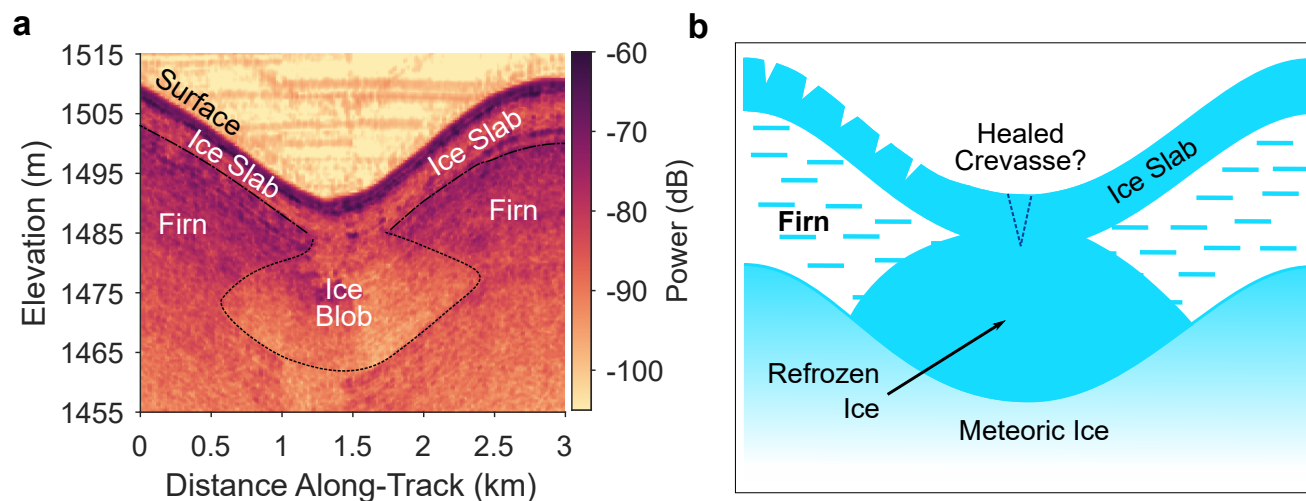


Fig. 1. Ice-penetrating radar observations of water storage beneath an ice slab in Northwest Greenland. a) Radar observations in 2016 show an ice blob that has refrozen in the porous firn beneath the ice slab. b) An idealized schematic of an ice blob, after Culberg and others (2022), where the initial crevasse that allowed for drainage is thought to be relatively shallow and to have healed as the ice blob refroze.

84 to resilience to hydrofracture (Bunger and others, 2005; Chen and others, 2022; Detournay, 2016; Meng
 85 and others, 2020, 2022, 2023). The observations of Culberg and others (2022) also highlight that even if a
 86 crevasse is filled with water, the presence of firn should instead limit fracture propagation. Therefore, the
 87 compressibility and permeability of firn need to be considered.

88 To address this challenge, here we develop a poromechanical model to predict the effective stress in the
 89 firn layer beneath a water-filled fracture in an ice slab. This approach can describe both fluid flow out of
 90 the fracture and the solid-fluid coupling that impacts stresses. Based on these simulations, we propose an
 91 analytical model for the maximum effective stress in the firn layer for both constant water pressure and
 92 constant injection rate conditions. We then apply this model to assess the vulnerability of Greenland's ice
 93 slab regions to hydrofracture and analyze the behavior of the system as a function of water availability, ice
 94 slab thickness, and the mechanical and hydraulic properties of the firn.

95 2. METHODS

96 In regions with high velocity gradients, dry surface fractures may form in ice slabs. If meltwater flows into
 97 these crevasses, they may continue to propagate until they reach the underneath permeable firn layer as
 98 shown in Figure 2. The meltwater then penetrates into the firn layer either by infiltration or fracturing.

99 Previous research has used two-phase continuum models to study meltwater flow through snow without
 100 considering flow-induced deformation in the porous snow layer (Meyer and Hewitt, 2017; Moure and others,
 101 2023). We develop a two-dimensional, poroelastic continuum model to quantify the stress and pressure
 102 changes in the firn layer during meltwater penetration (Biot, 1941; Wang, 2000; Coussy, 2004). Here, we
 103 consider two scenarios of water infiltration into the porous firn layer:

- 104 1. Constant pressure boundary condition : a constant water height (H_w) in the surface crevasse.
- 105 2. Constant flow rate boundary condition: a constant water injection velocity (V_{inj}) at the crevasse tip.

When stress is applied to porous media, part of the stress is transmitted through the pore fluid and part of the stress is transmitted through the solid skeleton. Effective stress (σ')—the fraction of the total stress (σ) that is transmitted through the solid skeleton—controls the mechanical behavior of porous media (Terzaghi, 1943). We assume the porous firn layer to be an isotropic, linear elastic continuum. Figure 2 shows the stresses acting on the firn layer from initial stresses and hydrostatic water pressure. We assume plane-strain condition for this 2D model ($\epsilon_{yy} = 0, \frac{\partial}{\partial y} = 0$). To rationalize the crossover from infiltration to fracturing regimes quantitatively, we adopt a fracturing criterion for cohesive porous media: the horizontal tensile effective stress (σ'_{xx}) should exceed the material tensile strength (σ'_t) to generate vertical fractures (Coussy, 2004; Wang, 2000). The criterion has been verified experimentally with hydrostone (Haimson and Fairhurst, 1969) and granular packs made of polyurethane (Meng and others, 2023). The fracture criterion at the crevasse tip (point A in Fig. 2) is written as follows:

$$\sigma'_{xx} = \sigma'_{xx,0} + \delta\sigma'_{xx} \geq \sigma'_t, \quad (1)$$

106 where $\sigma'_{xx,0}$ is the initial horizontal effective stress before water infiltration, $\delta\sigma'_{xx}$ is the infiltration-induced
 107 effective stress, and σ'_t is the tensile strength of firn that ranges from 45 kPa to 1 MPa with the density
 108 increasing from 500 kg m^{-3} to 900 kg m^{-3} (Petrovic, 2003; Shimaki and Arakawa, 2021).

109 2.1 Initial effective stresses before water infiltration

Before water penetrates into the surface crevasses, the firn layer has atmospheric pore pressure ($p_0 = 0$), and the effective stress is equal to the total stress. We first derive the expression for the initial effective stress in the firn layer without the presence of water, $\sigma'_{xx,0}$. Terzaghi's effective stress tensor σ' is the portion of the stress supported through deformation of the solid skeleton, and here we adopt the convention of

tension being positive. The stress–strain constitutive equation for the linear elastic firn layer is:

$$\boldsymbol{\sigma}' = \frac{3K\nu}{1+\nu}\epsilon_{kk}\mathbf{I} + \frac{3K(1-2\nu)}{1+\nu}\boldsymbol{\epsilon}, \quad (2)$$

where K , ν , $\boldsymbol{\epsilon}$ are the drained bulk modulus, the drained Poisson ratio of the firn layer (Biot, 1941; Terzaghi, 1943), and the strain tensor, respectively. The constitutive equations for plane-strain are obtained by inserting the constraint that $\epsilon_{yy} = 0$ into Eqn. (2) and noting that $\epsilon_{kk} = \epsilon_{xx} + \epsilon_{zz}$:

$$\sigma'_{xx,0} = \frac{3K\nu}{1+\nu}(\epsilon_{xx,0} + \epsilon_{zz,0}) + \frac{3K(1-2\nu)}{1+\nu}\epsilon_{xx,0}, \quad (3)$$

$$\sigma'_{zz,0} = \frac{3K\nu}{1+\nu}(\epsilon_{xx,0} + \epsilon_{zz,0}) + \frac{3K(1-2\nu)}{1+\nu}\epsilon_{zz,0}. \quad (4)$$

Solving Eqn. (4) for $\epsilon_{zz,0}$ and substituting into Eqn. (3) yields

$$\sigma'_{xx,0} = \frac{\nu}{1-\nu}\sigma'_{zz,0} + \frac{3K(1-2\nu)}{(1+\nu)(1-\nu)}\epsilon_{xx,0}. \quad (5)$$

Eqn. (5) gives the initial effective lateral stresses at the crevasse tip (point A in Figure 2):

$$\sigma'_{xx,0} = -\frac{\nu}{1-\nu}\rho_i g H_i + \frac{3K(1-2\nu)}{(1+\nu)(1-\nu)}\epsilon_{xx,0}, \quad (6)$$

110 where ρ_i , H_i are the density and height of the ice slab above the firn layer, respectively. By assuming
 111 linear elasticity for the porous firn layer under plane-strain conditions, the initial horizontal effective stress
 112 is partitioned into the lithostatic stress and the extensional/compressional stress induced by the horizontal
 113 strain due to ice flow.

114 2.2 Water infiltration into the porous firn layer

Following Coussy (2004), the poroelasticity equation states that

$$\delta\boldsymbol{\sigma} = \delta\boldsymbol{\sigma}' - b\delta p\mathbf{I}, \quad (7)$$

115 where $\delta\boldsymbol{\sigma}$, $\delta\boldsymbol{\sigma}'$, δp are the infiltration-induced changes in the Cauchy total stress tensor, the effective stress
 116 tensor, and the pore pressure, respectively, and $b \in [0, 1]$ is the Biot coefficient of the porous medium. We

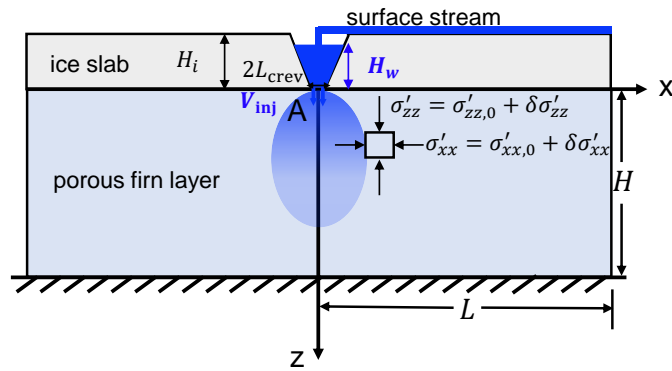


Fig. 2. A schematic showing stresses acting on the porous firn layer during water infiltration from the crevasse.

117 then derive the expression for the infiltration-induced horizontal effective stress, $\delta\sigma'_{xx}$. Figure 2 shows the
 118 stresses acting on the firn layer with water injection through a crevasse with an opening width of $2L_{crev}$
 119 and either a constant water height in the crevasse (H_w) or constant water injection velocity (V_{inj}). To
 120 quantify the stresses and pressure changes during the water infiltration into the dry cohesive firn layer,
 121 we develop a two-dimensional, two-phase poroelastic continuum model. In the following, we present the
 122 extension of Biot's theory to two-phase flow (Jha and Juanes, 2014; Bjørnarå and others, 2016), where we
 123 consider small deformations.

124 *2.2.1 Geomechanical equations*

Under quasi-static conditions, the balance of linear momentum leads to the equation of equilibrium as follows:

$$\nabla \cdot (\boldsymbol{\sigma}_0 + \delta\boldsymbol{\sigma}) + (\rho_{b,0} + \delta\rho_b)\mathbf{g} = \mathbf{0}, \tag{8}$$

125 where \mathbf{g} is gravitational acceleration, $\boldsymbol{\sigma}_0$ is the initial total stress before water infiltration, $\delta\boldsymbol{\sigma}$ is the
 126 infiltration-induced change in the total stress, and $\rho_{b,0}$ is the initial bulk density before water infiltration,
 127 $\rho_{b,0} = (1 - \phi)\rho_s + \phi\rho_a$. The infiltration-induced change in the bulk density for the solid-fluid system is
 128 $\delta\rho_b = (\rho_w - \rho_a)\phi S_w$ (Bjørnarå and others, 2016), where ρ_s is the solid ice density, ϕ is the porosity, and
 129 ρ_α and $S_\alpha \in [0, 1]$ are the density and saturation of the fluid phase α (water w or air a), respectively.

We obtain the differential form by subtracting static initial conditions from Eqn. (8):

$$\nabla \cdot (\delta\boldsymbol{\sigma}) + (\delta\rho_b)\mathbf{g} = \mathbf{0}. \tag{9}$$

The 2D stress balance equation becomes:

$$\begin{aligned} \frac{\partial(\delta\sigma_{xx})}{\partial x} + \frac{\partial(\delta\sigma_{zx})}{\partial z} &= 0, \quad \text{in x direction,} \\ \frac{\partial(\delta\sigma_{xz})}{\partial x} + \frac{\partial(\delta\sigma_{zz})}{\partial z} + (\delta\rho_b)g &= 0, \quad \text{in z direction.} \end{aligned} \quad (10)$$

The infiltration-induced strain tensor is defined as $\delta\boldsymbol{\epsilon} = \frac{1}{2}[\nabla\mathbf{u} + (\nabla\mathbf{u})^T]$, where $\mathbf{u} = [u, y, w]$ is the infiltration-induced displacement vector, and u, y , and w are the displacements in x, y, z directions, respectively. For 2D deformation in plane-strain condition, the strains are written as:

$$\delta\epsilon_{xx} = \frac{\partial u}{\partial x}, \quad \delta\epsilon_{zz} = \frac{\partial w}{\partial z}, \quad \delta\epsilon_{xz} = \frac{1}{2}\left(\frac{\partial u}{\partial z} + \frac{\partial w}{\partial x}\right), \quad \delta\epsilon_{kk} = \delta\epsilon_{xx} + \delta\epsilon_{zz}. \quad (11)$$

130 Using equations (7), (2), and (11), the stress balance equation (10) can be expressed as a function of
 131 infiltration-induced displacements $u(x, z, t)$, $w(x, z, t)$, the infiltration-induced change in the pore pressure
 132 $\delta p(x, z, t)$, and the saturation of the water phase $S_w(x, z, t)$.

133 2.2.2 Fluid flow equations

For the two-phase immiscible flow system, the conservation of fluid mass can be written as follows:

$$\frac{\partial(\phi\rho_\alpha S_\alpha)}{\partial t} + \nabla \cdot (\rho_\alpha \phi S_\alpha \mathbf{v}_\alpha) = 0. \quad (12)$$

The phase velocity \mathbf{v}_α is related to the Darcy flux \mathbf{q}_α in a deforming medium by the following relation:

$$\mathbf{q}_\alpha = \phi S_\alpha (\mathbf{v}_\alpha - \mathbf{v}_s) = -\frac{k_0}{\eta_\alpha} k_{r\alpha} (\nabla(\delta p_\alpha) - \rho_\alpha \mathbf{g}), \quad (13)$$

where \mathbf{v}_s is the velocity of the solid phase, k_0 is the intrinsic permeability of the porous firn layer, \mathbf{g} is the gravity vector, and η_α , $k_{r\alpha} = k_{r\alpha}(S_\alpha)$ and δp_α are the dynamic viscosity, relative permeability, and infiltration-induced fluid pressure for phase α (water w or air a), respectively. As the initial fluid pressure in the dry firn layer is $p_0 = 0$ before water infiltration, the total fluid pressure equals to infiltration-induced fluid pressure, $p_\alpha = \delta p_\alpha$. Since capillary pressure is negligible here, ($p_c = p_w - p_a = 0$) the two phases have the same fluid pressure p . The relative permeability functions are given as Corey-type power law functions

(Meyer and Hewitt, 2017; Moure and others, 2023):

$$k_{rw} = S_w^{a_w} \quad \text{and} \quad k_{ra} = (1 - S_w)^{a_a}, \quad (14)$$

134 where the fitting parameters are the exponents $a_w = 3$ and $a_a = 2$ (Bjørnarå and others, 2016).

The mass conservation equation for the solid phase is given below:

$$\frac{\partial[\rho_s(1 - \phi)]}{\partial t} + \nabla \cdot [\rho_s(1 - \phi)\mathbf{v}_s] = 0. \quad (15)$$

Assuming isothermal conditions and using the equation of state for the solid, the following expression for the change in porosity is obtained (Lewis and Schrefler, 1999):

$$\frac{\partial\phi}{\partial t} = (b - \phi) \left(c_s \frac{\partial(\delta p)}{\partial t} + \nabla \cdot \mathbf{v}_s \right), \quad (16)$$

where c_s is the compressibility of the solid phase, $b \in [0, 1]$ is the Biot coefficient of the porous medium. Combining equations (13) and (16), we expand equation (12) and arrive at the governing equation for two phase fluids (see details of algebra in the Supplementary Material):

$$\phi \frac{\partial S_\alpha}{\partial t} + S_\alpha \left(b \frac{\partial(\delta\epsilon_{kk})}{\partial t} + (\phi c_\alpha + (b - \phi)c_s) \frac{\partial(\delta p)}{\partial t} \right) + \nabla \cdot \mathbf{q}_\alpha = 0, \quad (17)$$

135 where c_α (Pa^{-1}) is the compressibility of fluid phase and $\delta\epsilon_{kk}$ is the infiltration-induced volumetric
136 strain of the solid phase.

Adding equation (17) for water and air phases, and imposing that $S_a + S_w \equiv 1$ for the porous firn layer, we obtain the pressure diffusion equation:

$$b \frac{\partial(\delta\epsilon_{kk})}{\partial t} + \frac{1}{M} \frac{\partial(\delta p)}{\partial t} + \nabla \cdot \mathbf{q}_t = 0, \quad (18)$$

137 where $\mathbf{q}_t = \mathbf{q}_w + \mathbf{q}_a$ is the total Darcy flux for water and air phases. The Biot modulus of the porous firn,
138 M , is related to fluid and firn properties as $\frac{1}{M} = \phi S_w c_w + \phi(1 - S_w)c_a + (b - \phi)c_s$, where c_w , c_a are the
139 water and air compressibility, respectively (Coussy, 2004).

140 2.2.3 Summary of governing equations

We use a 2D, two-phase poroelastic continuum model to solve the infiltration-induced stress and pressure changes. The model has four governing equations, two derived from conservation of fluid mass [Eqn. (18) for the water–air fluid mixture and Eqn. (17) for the water phase] and two derived from conservation of linear momentum [Eqn. (10)]. After applying the constitutive law [Eqn. (2)] and the definition of the effective stress [Eqn. (7)], stresses in Eqn. (10) are expressed in terms of displacements and pore pressure. The model solves the time evolution of four unknowns: (1) pore pressure field $\delta p(x, z, t)$; (2) water saturation field $S_w(x, z, t)$; (3) horizontal displacement field $u(x, z, t)$, and (4) vertical displacement field $w(x, z, t)$ of the porous firn layer. The governing equations are summarized and written in x, z coordinates as follows:

$$\begin{aligned}
 & b \frac{\partial(\delta\epsilon_{kk})}{\partial t} + \frac{1}{M} \frac{\partial(\delta p)}{\partial t} - k_0 \frac{\partial}{\partial x} \left(\left(\frac{k_{rw}}{\eta_w} + \frac{k_{ra}}{\eta_a} \right) \frac{\partial(\delta p)}{\partial x} \right) \\
 & - k_0 \frac{\partial}{\partial z} \left(\left(\frac{k_{rw}}{\eta_w} + \frac{k_{ra}}{\eta_a} \right) \frac{\partial(\delta p)}{\partial z} - \left(\frac{\rho_w k_{rw}}{\eta_w} + \frac{\rho_a k_{ra}}{\eta_a} \right) g \right) = 0,
 \end{aligned} \tag{19}$$

$$\begin{aligned}
 \phi \frac{\partial S_w}{\partial t} + S_w \left(b \frac{\partial(\delta\epsilon_{kk})}{\partial t} + (\phi c_w + (b - \phi) c_s) \frac{\partial(\delta p)}{\partial t} \right) - \frac{k_0}{\eta_w} \frac{\partial}{\partial x} \left(k_{rw} \frac{\partial(\delta p)}{\partial x} \right) \\
 - \frac{k_0}{\eta_w} \frac{\partial}{\partial z} \left(k_{rw} \left(\frac{\partial(\delta p)}{\partial z} - \rho_w g \right) \right) = 0,
 \end{aligned} \tag{20}$$

$$\frac{\partial}{\partial x} \left(\frac{3K\nu}{1+\nu} \delta\epsilon_{kk} + \frac{3K(1-2\nu)}{1+\nu} \delta\epsilon_{xx} - b\delta p \right) + \frac{\partial}{\partial z} \left(\frac{3K(1-2\nu)}{1+\nu} \delta\epsilon_{xz} \right) = 0, \tag{21}$$

$$\frac{\partial}{\partial x} \left(\frac{3K(1-2\nu)}{1+\nu} \delta\epsilon_{xz} \right) + \frac{\partial}{\partial z} \left(\frac{3K\nu}{1+\nu} \delta\epsilon_{kk} + \frac{3K(1-2\nu)}{1+\nu} \delta\epsilon_{zz} - b\delta p \right) + (\delta\rho_b)g = 0, \tag{22}$$

141 where $\delta\epsilon_{xx} = \frac{\partial u}{\partial x}$, $\delta\epsilon_{zz} = \frac{\partial w}{\partial z}$, $\delta\epsilon_{xz} = \frac{1}{2} \left(\frac{\partial u}{\partial z} + \frac{\partial w}{\partial x} \right)$, $\delta\epsilon_{kk} = \delta\epsilon_{xx} + \delta\epsilon_{zz}$.

142 Solving the four coupled governing equations [Eqns.(19), (20), (21), (22)], we obtain the spatiotemporal
 143 evolution of the saturation, displacements and pressure field. To quantify the vulnerability of firn to
 144 hydrofractures based on Eqn. (1), the model outputs the infiltration-induced change of horizontal effective
 145 stress as follows:

$$\delta\sigma'_{xx} = \frac{3K\nu}{1+\nu} \delta\epsilon_{kk} + \frac{3K(1-2\nu)}{1+\nu} \delta\epsilon_{xx}. \tag{23}$$

146 2.2.4 Initial and boundary conditions

The model solves the infiltration-induced pressure and stress changes in the porous firn layer, where $0 \leq x \leq L$, and $0 \leq z \leq H$ as shown in Figure 2. Water flows into the crevasse, the tip of which has an opening L_{crev} . Water infiltrates into the porous firn layer via the crevasse tip at either a constant height, H_w , or a constant velocity, V_{inj} . We initialize the model by specifying $u(x, z, 0) = w(x, z, 0) = \delta p(x, z, 0) = 0$. The water saturation is zero everywhere except at the crevasse tip, where it is kept at $S_w = 1$ as follows:

$$S_w(x \leq L_{\text{crev}}, 0, t) = 1, S_w(x > L_{\text{crev}}, 0, t) = S_w(x, z > 0, 0) = 0. \quad (24)$$

We consider the stress (or displacement) and pressure (or flow rate) boundary conditions on the domain area. On the left boundary ($x = 0$), axis of symmetry requires that $\frac{\partial}{\partial x} = 0$, and horizontal displacement equals zero. On the right boundary, we assume it is far from the crevasse tip and unaffected by the infiltration. On the bottom boundary where the firn layer touches the impermeable, rigid ice column, the displacements and vertical water flow rate are zero. On the top boundary, when the water surface height exceeds the ice slab height (e.g. when a lake overlies the ice slab), the lake depth adds to the initial lithostatic stresses. Otherwise the overlying ice slab provides constant lithostatic stresses. The vertical water flowrate is zero everywhere except at the crevasses, where either $\delta p = \rho_w g H_w$ or $q_{w,z} = V_{\text{inj}}$. The boundary conditions are summarized as follows:

$$\begin{aligned} u|_{x=0} = \frac{\partial w}{\partial x}|_{x=0} = \frac{\partial p}{\partial x}|_{x=0} = \frac{\partial S_w}{\partial x}|_{x=0} = 0, \\ u|_{x=L} = w|_{x=L} = \delta p|_{x=L} = 0, \\ u|_{z=H} = w|_{z=H} = q_{w,z}|_{z=H} = 0, \\ \delta \sigma'_{xx}|_{z=0} = 0, \\ \delta \sigma'_{zz}|_{z=0} = 0, \\ q_{w,z}|_{z=0}(x > L_{\text{crev}}) = 0, \\ \delta p|_{z=0}(x \leq L_{\text{crev}}) = \rho_w g H_w \quad \text{or} \quad q_{w,z}|_{z=0}(x \leq L_{\text{crev}}) = V_{\text{inj}}. \end{aligned} \quad (25)$$

Table 1. Modeling parameters for the 2D, two-phase poroelastic continuum model

Symbol	Value	Unit	Variable
L	30	m	Length of the firn layer
H	30	m	Height of the firn layer
L_{crev}	2	m	Half of the opening of the crevasse
H_w	10	m	Water height above the firn layer
V_{inj}	0.05	m s^{-1}	Water infiltration rate
c_w	5×10^{-10}	Pa^{-1}	Water compressibility
c_a	7×10^{-6}	Pa^{-1}	Air compressibility
c_s	1.25×10^{-10}	Pa^{-1}	Ice grain compressibility
K	4	GPa	Bulk modulus of the firn layer
K_s	8	GPa	Bulk modulus of the ice grain
ν	0.3		Poisson ratio of the firn layer
b	0.5		Biot coefficient of the firn layer
η_w	0.001	Pa s	Injecting water viscosity
η_a	1.8×10^{-5}	Pa s	Air viscosity
ϕ	0.2		Porosity of the firn layer
k_0	10^{-9}	m^2	Intrinsic permeability of the firn layer
ρ_w	997	kg m^{-3}	Density of water
ρ_a	1.23	kg m^{-3}	Density of air

147 2.2.5 Model parameters

148 The four poroelastic constants in the model are the drained bulk modulus K , the drained Poisson ratio ν ,
 149 the Biot coefficient b , and the Biot modulus M of the firn layer. We calculate the Biot coefficient from the
 150 relationship $b = 1 - \frac{K}{K_s}$ (Coussy, 2004), where K_s is the bulk modulus of the ice grain. The Biot modulus
 151 of the porous firn, M , is related to fluid and firn properties as $\frac{1}{M} = \phi S_w c_w + \phi(1 - S_w)c_a + (b - \phi)c_s$
 152 (Coussy, 2004), which is a spatiotemporal variable as water penetrates into the firn layer. A summary of
 153 the modeling parameters is given in Table 1.

154 2.2.6 Numerical implementation

155 We use a finite volume numerical scheme to solve the four coupled governing equations [Eqns. (19), (20), (21),(22)].

156 We sequentially solve time-discretized equations within a timestep. We update the flow and mechanics

157 simultaneously [Eqns. (19), (21), (22)] using implicit time discretization, and separately from the saturation
158 by treating the saturation as a fixed variable. Then we solve the water transport equation [Eqn. (20)] with
159 prescribed pressure and displacement fields. By the end of each timestep, the four unknown quantities
160 are all updated. See the Supplementary Material for the convergence and mesh independence analysis.
161 The modeling results reach convergence with the mesh size $dx=dz=0.5$ m, which is adopted for all the
162 simulation presented here.

163 3. MODELING RESULTS

164 3.1 Spatiotemporal evolution of pressures and stresses

165 Figures 3 and 4 compare our modeling results for water infiltration with two different boundary conditions
166 at the crevasse tip: constant pressure ($H_w = 10$ m), and constant flow rate ($V_{inj} = 0.05$ m s⁻¹). In
167 both cases, water infiltrates into the porous firn layer due to the pressure gradient and gravity, resulting
168 in an elliptical-like shape for the water saturation profile as shown in Figure 3(a). Figure 3(b) presents
169 the temporal evolution of the pore pressure field, highlighting the pressure diffusion within the water
170 phase. The viscous dissipation is constrained within a certain depth, below which the water flow becomes
171 purely gravity-driven. Figure 3(c) shows the spatiotemporal evolution of the infiltration-induced horizontal
172 effective stress change ($\delta\sigma'_{xx}(x, z, t)$). At the crevasse tip, the firn is under the maximum tensile effective
173 stress, which makes it the most vulnerable place for hydrofracturing (see the fracture criterion in Eqn. (1)).

174 Figure 4 presents the temporal evolution of the infiltration-induced pore pressure ($P_{inj}(t)$) and the
175 effective stress ($\delta\sigma'_{xx}(t)$) at the crevasse tip. For the constant velocity injection condition, Figure 4(a) shows
176 that it takes some time for the injection pressure to build up, and thus the water invading front is slightly
177 delayed compared with the constant pressure condition. With either constant pressure or constant flow rate
178 as the boundary condition, Figure 4(b) shows that the tensile effective stress at the crevasse tip experiences
179 a logarithmic-like growth in time with a fast increase in the first 30 seconds. To avoid boundary effects, we
180 terminate the simulation when water infiltrates into half of the domain depth, and take the corresponding
181 pressure (δp) and tensile effective stress at the crevasse tip ($\delta\sigma'_{xx,max}$) for the following scaling analysis. To
182 confirm that the effective stress does not increase noticeably as infiltration keeps going, we have extended
183 the simulation time and find that the effective stress value we choose effectively captures its maximum
184 value developed during infiltration (see Supplementary Material).

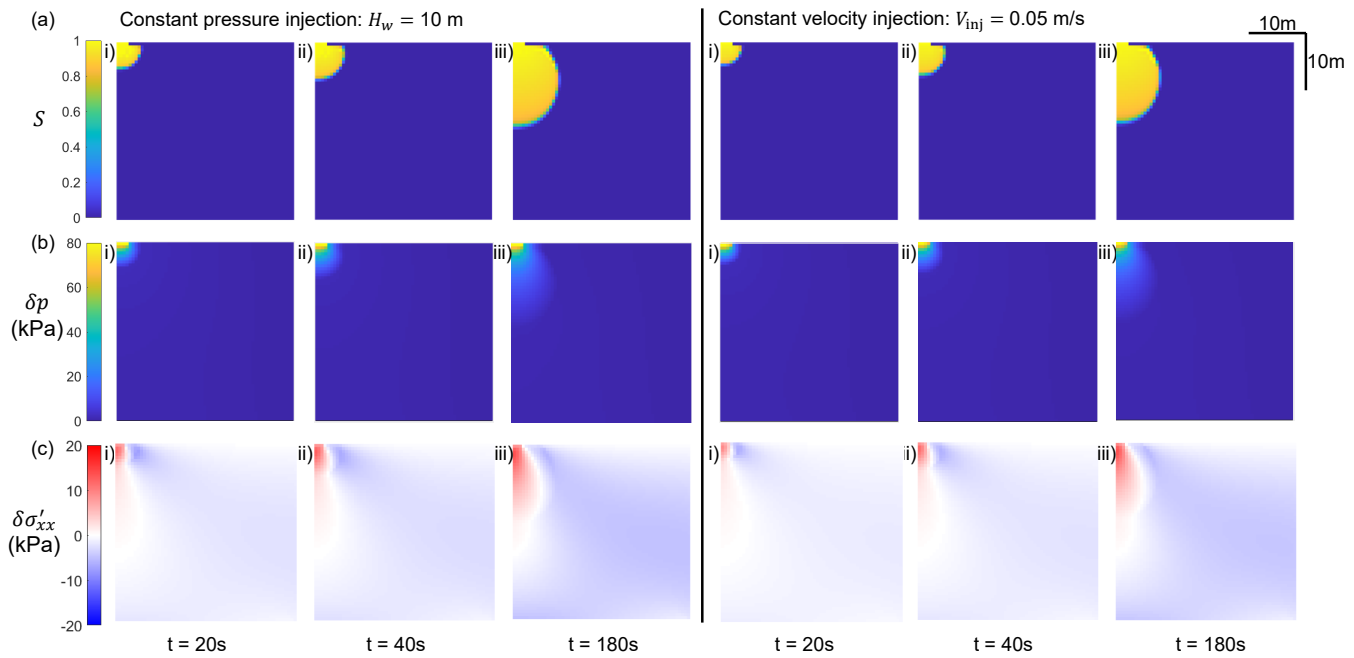


Fig. 3. Modeling results for the water infiltration with $H_w = 10$ m (left panel), $V_{inj} = 0.05$ m s⁻¹ (right panel) in the domain $0 < x < L$, $0 < z < H$, where $L = H = 30$ m. A sequence of snapshots shows the spatiotemporal evolution of (a) water saturation field, $S_w(x, z, t)$, (b) pore pressure field, $\delta p(x, z, t)$, and (c) infiltration-induced horizontal effective stress change, $\delta\sigma'_{xx}(x, z, t)$. Infiltration time $t=20$ s, 40s, 180s from snapshot i), ii) to iii).

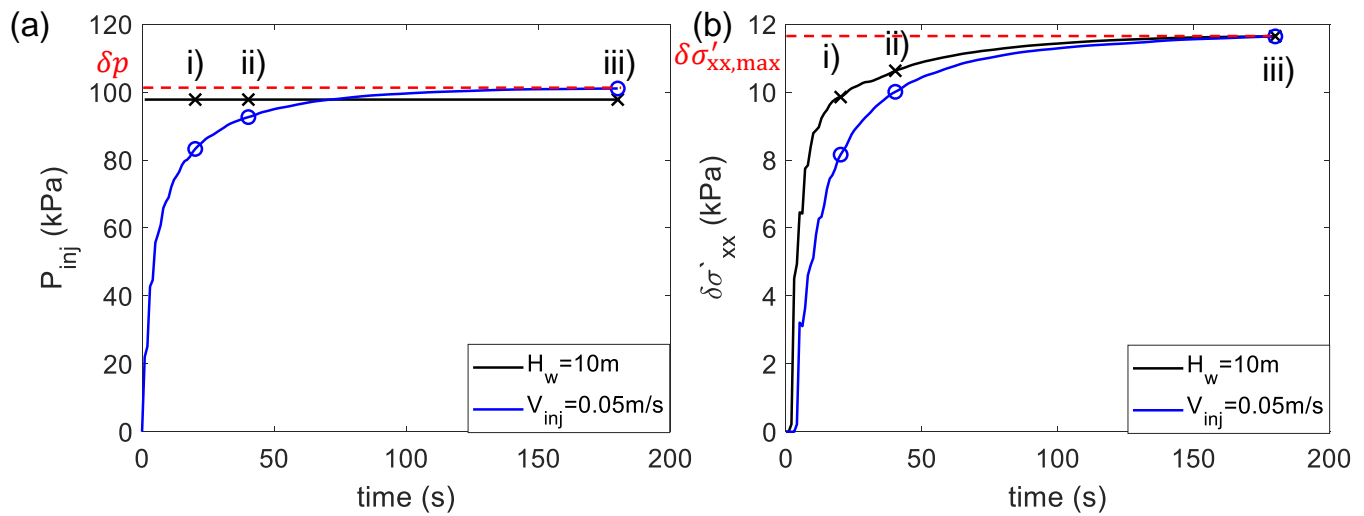


Fig. 4. Modeling results for the water infiltration with $H_w = 10$ m (black line) and $V_{inj} = 0.05$ m s⁻¹ (blue line). Time evolution of (a) injection pressure $P_{inj}(t)$ at the crevasse tip, and (b) infiltration-induced horizontal effective stress change at the crevasse tip $\delta\sigma'_{xx}(t)$. We use their maximum values (δp , $\delta\sigma'_{xx,max}$) to evaluate the vulnerability of the porous firn layer to hydrofracturing. The markers indicate times for the snapshots shown in Figure 3: $t=20$ s, 40s, 180s in sequence.

185 3.2 Analytical model

186 3.2.1 Scaling between $\delta\sigma'_{xx,max}$ and δp

To check whether fracture initiates in the porous firn layer during meltwater infiltration, we focus on the stress and pressure changes at the crevasse tip, which has been shown to be the most vulnerable place. To implement the fracture criterion in Eqn. (1) more efficiently, we develop a scaling relationship between $\delta\sigma'_{xx,max}$ and δp , which dictates how much of the infiltration-induced pore pressure change is transmitted to the solid skeleton. We recall the poroelasticity equation for the effective stress [Eqn. (7)], and propose a scaling law for the infiltration-induced horizontal effective stress change at the crevasse tip as follows:

$$\delta\sigma'_{xx,max} = \delta\sigma_{xx,max} + b\delta p = -\gamma(b\delta p) + (b\delta p) = \beta(b\delta p), \quad (26)$$

187 where we assume the horizontal total stress change is linearly proportional to the pore pressure change
 188 with a numerical pre-factor $0 < \gamma < 1$, and is negative as it is compressive. We then conduct a series of
 189 simulations to determine the numerical pre-factor $0 < \beta < 1$.

190 We conduct a series of simulation under constant injection pressure or constant injection velocity
 191 boundary conditions by varying the modeling parameters, including $b, H_w, V_{inj}, L_{crev}$ and k_0 . We set $H_w <$
 192 H_i in all simulations with a constant pressure boundary condition. Figure 5 shows that when we combine
 193 all the numerical data of $\delta\sigma'_{xx,max}$ and δp onto a single plot, our proposed scaling is robust across a range
 194 of parameters and both boundary conditions: $\delta\sigma'_{xx,max} = \beta(b\delta p)$, where $\beta = 0.22$.

195 3.2.2 The analytical expression of δp

To find the modeling parameters that impact the stresses, we develop analytical predictions of δp under the two boundary conditions. For the constant pressure injection at the crevasse tip, the pressure change is equal to the hydrostatic water pressure, $\delta p = \rho_w g H_w$. For the constant velocity injection at the crevasse tip, we derive δp from fluid continuity and Darcy's law. We assume that above a certain water infiltration depth H_0 , whose expression is derived later, water infiltrates much faster than the hydraulic conductivity of the firn. Therefore gravity is negligible and water invades in an approximately radially symmetric manner as shown in Figure 3(i)(ii). We approximate the flow near the tip as spreading out from the initial crack

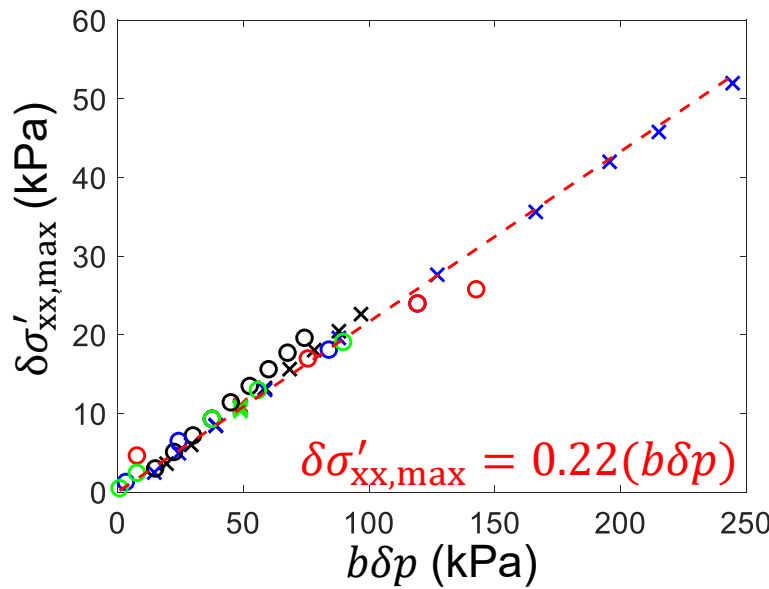


Fig. 5. The scaling between $\delta\sigma'_{xx,max}$ and $b\delta p$ retrieved from simulations. Markers represent all simulation data in Figure 7 from water infiltration with a constant injection pressure (cross markers) or constant injection velocity (circular markers). We use the same colors and markers as Figure 7 for each simulation. The black, blue, red, green marker color represents a range of b , H_w or V_{inj} , L_{crev} , and k_0 , respectively. The dashed red line represents the analytical prediction: $\delta\sigma'_{xx,max} = \beta\delta p$ (Eqn. (26)), with the prefactor β fitted to be 0.22.

width L_{crev} at an angle θ . From the fluid continuity, we obtain:

$$V_{inj}L_{crev} = V(r)(L_{crev} + \theta r) \rightarrow V(r) = \frac{V_{inj}L_{crev}}{L_{crev} + \theta r}, \tag{27}$$

where $V(r)$ is the radial velocity for water at distance r from the crevasse tip. At $r = H_0$, the water velocity decays to the gravity-driven flow rate, which is also the hydraulic conductivity of water flow in porous firn. We derive the expression for H_0 as follows:

$$V(H_0) = V_{grav} = \frac{\rho_w g k_0}{\eta_w} \rightarrow H_0 = \frac{L_{crev}}{\theta} \left(\frac{\eta_w V_{inj}}{\rho_w g k_0} - 1 \right). \tag{28}$$

Pore pressure diffuses from the crevasse tip ($r = 0$) to H_0 , below which the flow becomes gravity-driven, resulting in the observed elliptical-like shape of the water invading front. We calculate the pressure diffusion

from $r = 0$ to H_0 by Darcy's law:

$$\begin{aligned} V(r) &= -\frac{k_0}{\eta_w} \frac{\partial p}{\partial r} \rightarrow \int_0^{H_0} -\frac{\eta_w}{k_0} V(r) \partial r = \int_{\delta p}^0 \partial p, \\ &\rightarrow \delta p = \frac{1}{\theta} \frac{\eta_w V_{\text{inj}} L_{\text{crev}}}{k_0} \ln\left(\frac{\eta_w V_{\text{inj}}}{\rho_w g k_0}\right). \end{aligned} \quad (29)$$

196 For all constant injection velocity simulations (Fig. 7(e)-(h)), we plot the simulated δp as a function
 197 of $\frac{\eta_w V_{\text{inj}} L_{\text{crev}}}{k_0} \ln\left(\frac{\eta_w V_{\text{inj}}}{\rho_w g k_0}\right)$ as markers in Figure 6, the slope of which implies the prefactor θ in Eqn. (29).
 198 We conclude that simulation results agree well with the theory [Eqn. (29)] when $\theta = 3\pi/5$. The inferred
 199 spreading angle θ is larger than $\pi/2$ because the infiltration front slightly deviates from a quarter circle
 200 under the effect of gravity. Note that Eqn. (29) applies to the condition when the water velocity decays to
 201 the gravity-driven flow rate before the invading front reaches approximately half of the domain depth. For
 202 an unrealistically large crevasse opening or water injection velocity at the crevasse tip, the invading front
 203 keeps expanding in a quarter circular-like shape, and H_0 in Eqn. (29) is replaced by the depth when we
 204 terminate the simulation ($\frac{H}{2}$ in this case). We include the analysis of large injection velocity or crevasse
 205 opening in the Supplementary Material. However, the large water pressure induced there (in the range of
 206 MPa) is not physical as it should have been capped by hydrostatic water pressure, $\rho_w g H_w$.

207 3.2.3 The analytical expression of $\delta\sigma'_{xx,\max}$

Now that we have the scaling between $\delta\sigma'_{xx,\max}$ and δp (Eqn. (26)), and the analytical expression of δp
 (Eqn. (29) with $\theta = 3\pi/5$), we arrive at the final analytical expression of infiltration induced maximum
 effective stress as follows:

$$\begin{aligned} \delta\sigma'_{xx,\max} &= \beta(b\delta p), \\ \delta p &= \begin{cases} \rho_w g H_w, & \text{with a constant } H_w, \\ \frac{5}{3\pi} \frac{\eta_w V_{\text{inj}} L_{\text{crev}}}{k_0} \ln\left(\frac{\eta_w V_{\text{inj}}}{\rho_w g k_0}\right), & \text{with a constant } V_{\text{inj}}. \end{cases} \end{aligned} \quad (30)$$

208 To check that Eqn. (30) holds for the conducted simulations, Figure 7 presents the dependence of $\delta\sigma'_{xx,\max}$
 209 on the modeling parameters, where the red dashed line represents the analytical prediction from Eqn. (30)
 210 with the numerical pre-factor β fitted to be 0.22.

Note that to cause fracture we need the maximum effective stress $\sigma'_{xx,\max} \equiv \sigma'_{xx,0} + \delta\sigma'_{xx,\max}$ to exceed
 the tensile strength σ'_t . Combining Eqn. (1), (6), and (30), we arrive at the final expression for the fracture

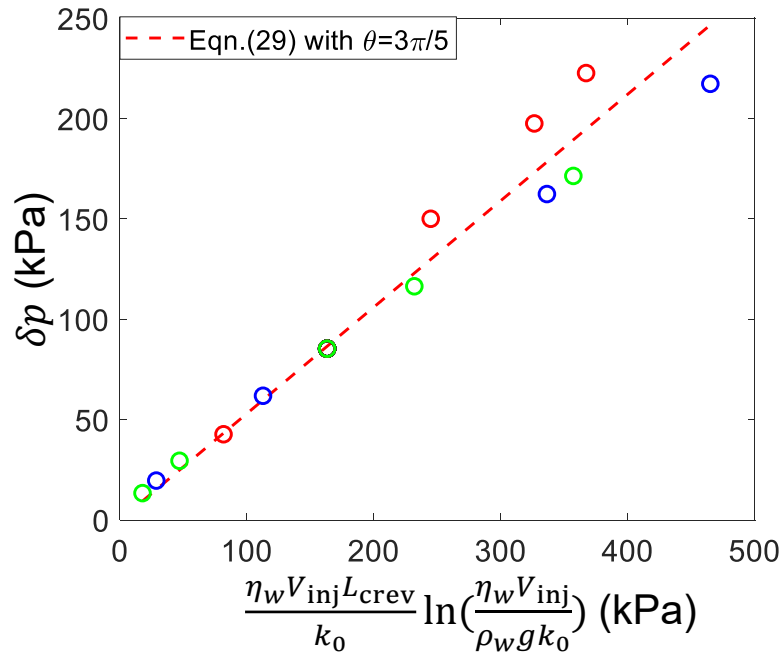
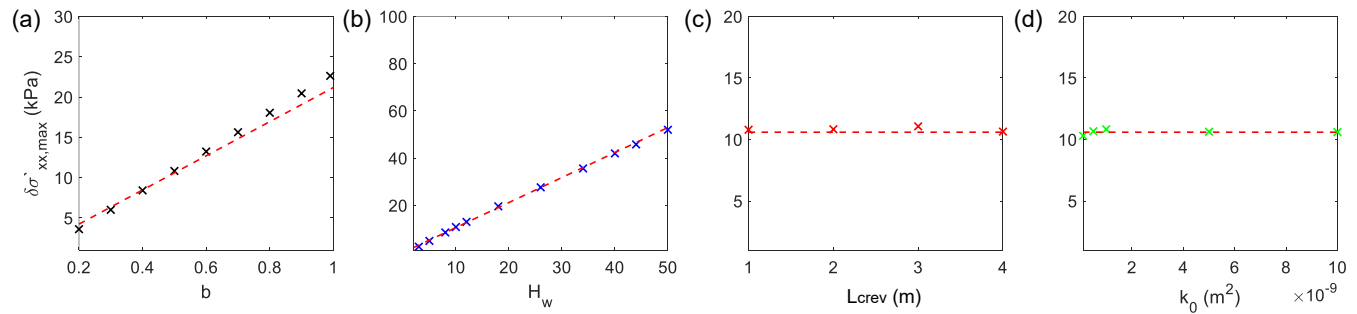


Fig. 6. The scaling between the infiltration-induced pore pressure change at the crevasse tip (δp) and viscous pressure ($\frac{\eta_w V_{inj} L_{crev}}{k_0} \ln(\frac{\eta_w V_{inj}}{\rho_w g k_0})$) from the water infiltration with a constant injection velocity. Circular markers represent simulation data in Figure 7 from water infiltration with a constant injection velocity. We use the same colors as Figure 7 for each simulation. The blue, red, green marker color represents a range of V_{inj} , L_{crev} , and k_0 , respectively. The red dashed line represents the analytical prediction from Eqn. (29) with $\theta = 3\pi/5$.

Constant pressure injection (H_w)



Constant velocity injection (V_{inj})

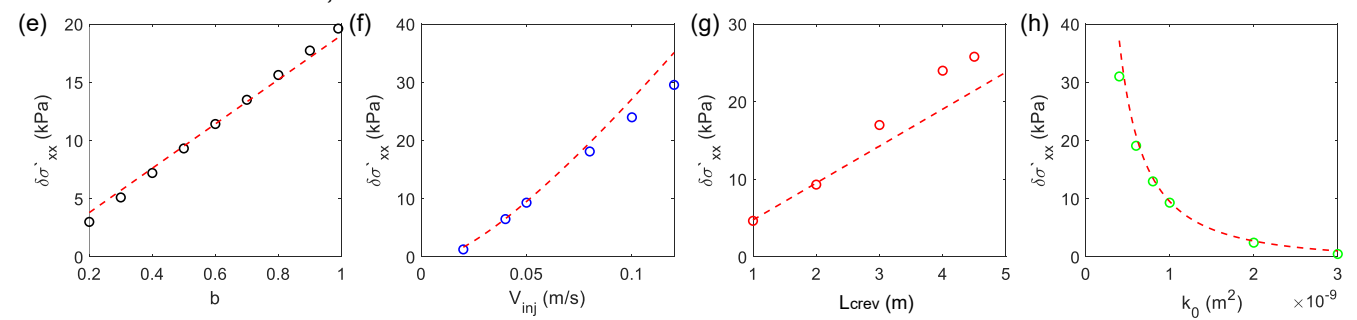


Fig. 7. The dependence of $\delta\sigma'_{xx,max}$ on modeling parameters ($b, H_w, V_{inj}, L_{crev}, k_0$) for the water infiltration with a constant injection pressure (top panels, (a)~(d)) and a constant injection velocity (bottom panels, (e)~(h)). On the top panel, $H_w = 10$ m except in (b), and on the bottom panel, $V_{inj} = 0.05$ m s⁻¹ except in (f). The markers represent simulation results, and the dashed red line represents analytical prediction from Eqn. (30) with $\beta = 0.22$.

criterion:

$$\sigma'_{xx,\max} = \sigma'_{xx,0} + \delta\sigma'_{xx,\max} = -\frac{\nu}{1-\nu}\rho_i g H_i + \frac{3K(1-2\nu)}{(1+\nu)(1-\nu)}\epsilon_{xx,0} - \frac{\nu}{1-\nu}\rho_w g \langle H_w - H_i \rangle + \beta(b\delta p) \geq \sigma'_t,$$

$$\delta p = \begin{cases} \rho_w g H_w, & \text{with a constant } H_w, \\ \frac{5}{3\pi} \frac{\eta_w V_{\text{inj}} L_{\text{crev}}}{k_0} \ln\left(\frac{\eta_w V_{\text{inj}}}{\rho_w g k_0}\right), & \text{with a constant } V_{\text{inj}}, \end{cases} \quad (31)$$

211 where $\langle x \rangle = \max(x, 0)$ follows the rule of Macaulay bracket. The third term in the expression of $\sigma'_{xx,\max}$
 212 accounts for additional background hydrostatic stress when there is ponding of the water on top of the ice
 213 slab. Figure 5 shows that the numerical pre-factor β is fitted to be 0.22.

214 3.3 Physical limits

215 Eqn. (31) provides different forms for the maximum effective stress in the firn depending on whether
 216 a constant pressure or constant injection velocity is assumed. Before applying this model to study the
 217 vulnerability of ice slab regions to hydrofracture, it is important to consider which boundary condition is
 218 most consistent with physical conditions on the ice sheet.

219 The constant pressure boundary condition straightforwardly represents a static water load in a partially
 220 or fully water-filled crevasse. It does not directly account for transient processes, such as water level
 221 fluctuations within a crevasse as water flows in from surface runoff or out through the permeable firn.
 222 However, by exploring the induced stresses for a range of water levels, we can constrain the plausible range
 223 of the maximum effective stress in the firn layer.

224 It is tempting to think of the constant injection velocity boundary condition as representing the transient
 225 case where water is flowing into the crevasse at a constant rate. However, this is not a good analogy. As
 226 Figure 4 shows, a constant injection rate leads to a roughly logarithmic-like increase in pressure with time,
 227 as more water is forced into the firn per time step than can be evacuated from the injection point due
 228 to the relatively low intrinsic permeability of the firn. However, a crevasse is not a closed system and
 229 the top remains open to the atmosphere. Therefore, when the rate of water injection into the crevasse
 230 exceeds the rate at which water can flow out through the firn, continuity of mass and pressure require
 231 that the water will start to fill the crevasse, rather than increase pressure in the firn layer. As a result,
 232 the constant injection rate boundary condition leads to artificially high estimates of firn pore pressure
 233 and, by extension, maximum effective stress, because our simulations assume a closed system and do not
 234 allow for backflow into the open crevasse. Therefore, we caution that the constant injection rate equations

Table 2. Monte Carlo Simulation Parameters

Variable	Distribution/Relation	Unit	Sources
ρ_i	$\mathcal{N}(873, 25)$	kg m^{-3}	Machguth and others (2016)
ρ_f	$\mathcal{U}[550, 800]$	kg m^{-3}	Machguth and others (2016); MacFerrin and others (2022)
H_i	Empirical distribution of all radar-observed ice slab thickness in Greenland	m	MacFerrin and others (2019)
H_w	$\mathcal{U}[0, H_i], (H_w \leq H_i)$ OR $\mathcal{U}[H_i + 0.1, H_i + 40], (H_w > H_i)$	m	Culberg and others (2022)
K	$K_\mu = (1.844 \times 10^{-5})\rho_f^2 - 0.006956\rho_f - 0.0606; \sigma_K = 0.436$	GPa	Schlegel and others (2019); King and Jarvis (2007); Smith (1965)
K_s	$\mathcal{N}(8.5, 0.28)$	GPa	Sayers (2021)
b	$b \equiv 1 - \frac{K}{K_s}$		Biot (1941)
ν	$\nu_\mu = 0.0002888\rho_f + 0.1005; \sigma_\nu = 0.0376$		Schlegel and others (2019); King and Jarvis (2007); Smith (1965)
k_0	$k_0 = 10^{-7.29}\phi_0^{3.71}$	m^2	Adolph and Albert (2014)

*Note that $\mathcal{N}(\mu, \sigma)$ denotes a normal distribution with mean μ and standard deviation σ and $\mathcal{U}[a, b]$ denotes a uniform distribution over the values from a to b (inclusive).

235 should not be used to calculate firn stresses. However, the constant injection rate model does provide an
 236 important relationship between pressure and injection velocity that we will later exploit to qualitatively
 237 estimate whether crevasses may fill with water, given typical stream flow rates into fractures.

238 4. APPLICATIONS TO THE GREENLAND ICE SHEET

239 We now apply the analytical model developed in Section 3 to assess the vulnerability of Greenland's ice
 240 slab regions to hydrofracture. To do this, we seek to answer the following questions:

- 241 1. Given typical firn conditions in Greenland, will fractures in ice slabs fill with water?
- 242 2. If so, does hydrostatic loading of an ice slab crevasse induce sufficient stress in the firn layer to initiate
 243 fracture?

244 The first question is important because, as water flows into the top of an ice slab crevasse, either from
 245 distributed hillslope flow or where a stream intersects the fracture, it will also flow out of the fracture tip
 246 into the permeable firn. If water can be evacuated into the firn about as quickly as it enters the crevasse,

247 the crevasse will not fill with water and there will be no additional hydrostatic stress that might drive
248 hydrofracture. However, if the rate of infiltration into the firn is smaller than the rate of injection into
249 the crevasse, the water level will rise within the crevasse. In this scenario, the second question becomes
250 relevant, and we can apply Eqn. 31 to determine whether, or under what conditions, the maximum effective
251 stress induced in the firn layer would be sufficient to initiate fracture.

252 4.1 Mechanical and hydraulic parameters

253 To answer these questions by applying the analytical model developed in Section 3, we must first define
254 reasonable values for the physical, mechanical, and hydraulic parameters of the ice slab-firn system in our
255 area of interest. Unfortunately, given the large spatial extent of ice slab regions, the sparsity of subsurface
256 observations within them, and the uncertainty in the few available measurements, it is difficult to choose
257 a single representative value for any of these parameters. Therefore, we take a Monte Carlo simulation
258 approach to this problem. For each variable, we define an empirical distribution of reasonable values using
259 a compilation of in situ, laboratory, and remote sensing measurements reported in the literature. For
260 the hydraulic and mechanical properties, which have never been measured directly in these regions, we
261 use various empirical relations to define these properties as a function of firn density. Table 2 lists these
262 unknown variables, the distributions we assign to them or the relation from which we calculate them, and
263 the sources on which we base these distributions or relations.

264 The relation between open porosity and firn permeability is taken from Adolph and Albert (2014),
265 which defined a power law relation between firn density and air permeability based on measurements from
266 firn core samples collected at the North GRIP ice core drill site. We define our own relations between
267 firn density and the mechanical parameters – Poisson ratio (ν) and Biot coefficient (b) – due to the lack
268 of reports in the literature. The Poisson ratio has been measured with ultrasonic wave velocities at the
269 laboratory scale and active seismic investigations at the field scale. We collate data sets from Schlegel
270 and others (2019), King and Jarvis (2007), and Smith (1965) and use Monte Carlo simulation to build an
271 expanded set of data points that cover the reported uncertainty for each measured data point. We then
272 calculate the best linear fit between firn density (ρ_f) and ν using this expanded data set [Supplementary
273 Figure 4] and define the uncertainty to be the one half of the 68% prediction interval on the measurements
274 (reported as σ_ν in Table 2). The Biot coefficient is defined as a function of the ratio between the bulk
275 modulus of the firn (K) and single grain elastic stiffness of ice (K_s). We define a relation between ρ_f and

276 K in the same way as we did for ν , but this time using a quadratic fit to bulk modulus data compiled from
 277 the same sources [Supplementary Figure 5].

278 We run two sets of Monte Carlo simulations, the first where H_w is always less than or equal to H_i and
 279 the second where H_w is always greater than H_i . At each iteration in each simulation, we first draw ρ_i ,
 280 ρ_f , L_{crev} , K_s , and H_i from the distributions defined in Table 2. If we are simulating a scenario in which
 281 we desire that $H_w \leq H_i$, we then draw H_w from the distribution $\mathcal{U}[0, H_i]$. Alternately, if we desire that
 282 $H_w > H_i$, we draw H_w from the distribution $\mathcal{U}[H_i + 0.1, H_i + 40]$. We use the randomly selected value
 283 of ρ_f to calculate K , ν , or k_0 as appropriate. For example, K is drawn from a distribution defined as
 284 $\mathcal{N}(K_\mu(\rho_f), \sigma_K)$ and then used to calculate b directly. For all the analyses that follow, we run 1,000,000
 285 iterations of the Monte Carlo simulation, equivalent to solving the equations summarized in Figure 9 for a
 286 million different plausible configurations of an ice slab-firn system. The output of this simulation process
 287 is a distribution of the physically plausible range of solutions to the equation we are solving, given what
 288 we know about conditions in Greenland's ice slab regions.

289 4.2 Rate of crevasse filling

To determine whether fractures in ice slabs can fill with water, we start with the constant injection velocity
 solution in Eqn. 31 which provides a relationship between pressure and firn infiltration velocity. This
 equation shows that the change in pore pressure is related to the injection velocity, crevasse opening width,
 and firn permeability. Since the crevasse is open to the atmosphere at its top, we know that the maximum
 possible pressure change in the firn would be the hydrostatic pressure induced by a water-filled crevasse.
 Therefore, we set Eqn. 31 equal to this hydrostatic pressure to estimate the maximum rate at which water
 can infiltrate into the firn.

$$\rho_w g H_w = \frac{5}{3\pi} \frac{\eta_w V_{\text{inj}} L_{\text{crev}}}{k_0} \ln\left(\frac{\eta_w V_{\text{inj}}}{\rho_w g k_0}\right). \quad (32)$$

290 Using the Monte Carlo approach described in Section 4.1, we numerically solve Eqn. 32 to compute a
 291 distribution of plausible infiltration rates (V_{inj}) into the firn beneath ice slabs.

We compare this distribution of infiltration rates to field measurements of supraglacial river and stream
 discharge to assess the balance between water flowing into and out of the crevasse. For this purpose, we
 reduce the system to two-dimensions and calculate discharge into the firn as follows:

$$Q_{\text{firn}} = V_{\text{inj}} L_{\text{crev}}. \quad (33)$$

We compare Q_{firn} ($\text{m}^2 \text{s}^{-1}$) to field observations of supraglacial stream and river discharge collected in the ablation zone of Southwest Greenland. Gleason and others (2016) measured width, depth, and discharge at 38 locations on a series of small streams – generally, less than 3m wide and 0.3 m deep. We calculate an equivalent 2D discharge by dividing the measured volumetric discharge by the stream width. Smith and others (2015) also developed a power law relation between stream width (w) and discharge (Q) shown in Eqn. 34 based on field measurements in the Southwest Greenland ablation zone.

$$Q = 0.099w^{1.85}. \quad (34)$$

292 To further estimate the range of plausible discharge rates for streams in ice slab regions, we measure the
293 width of a series of representative streams in the Northwest and Southwest Greenland ice slab areas using
294 WorldView imagery, making 3-5 measurements per stream (see Supplementary Figure 6). Measured stream
295 widths vary from 0.7-17 m, values which fall comfortably within the range of stream widths originally used
296 to calibrate Eqn. 34 (Smith and others, 2015). We use Eqn. 34 to calculate the estimate discharge of these
297 streams and rescale by the measured width to obtain equivalent 2D discharge. To ensure a conservative
298 estimate of stream discharge, we limit this calculation to stream widths between 0.7-8 m.

299 Figure 8 shows the results of this analysis. The blue histogram shows the rate at which water would
300 drain out of a crevasse in an ice slab into the underlying firn Q_{firn} , and the red histogram shows the
301 rate at which water can drain into the crevasse from the surface based on the Gleason and others (2016)
302 measurements. The gray shaded region shows the range of discharge rates calculated from our measured
303 stream widths using Eqn. 34. We do not plot these values as a histogram, since we do not sample a
304 sufficient number of streams to accurately capture the true distribution of stream widths in the region.
305 However, we can bound the reasonable range of stream discharge from these selected observations. This
306 analysis demonstrates two possible regimes. Q_{surf} and Q_{firn} are similar for the streams with the lowest
307 discharge rates and crevasses with the largest openings, highest pressures, and most permeable underlying
308 firn. This suggests that where crevasses are fed by small streams or hillslope flow, no hydrofracture will
309 occur because water drains into the firn as quickly as it enters the crevasse, and therefore no hydrostatic
310 stress is induced by water within the crevasse itself. However, we also see that the discharge from larger
311 streams (> 3 m wide) may be significantly greater than the rate at which water can drain out of a crevasse
312 into the firn. In this second regime, the crevasse will fill with water, leading to an additional hydrostatic
313 load that might be sufficient to vertically propagate the crevasse into the firn layer. We note that it is

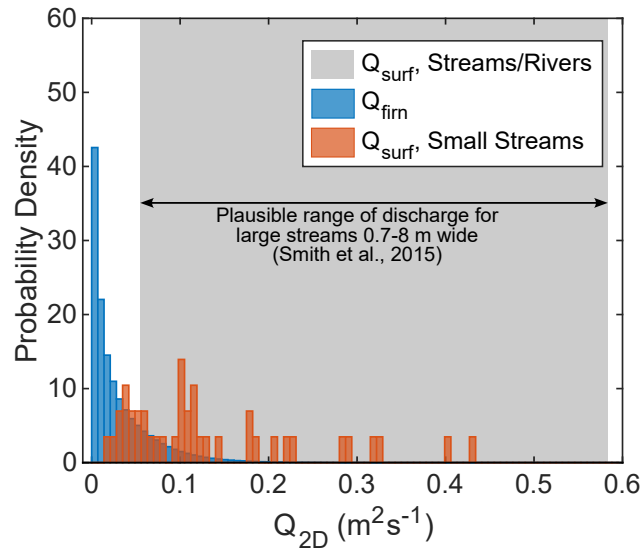


Fig. 8. Comparison of the rate of water infiltration into the firn from the crevasse tip versus the rate at which surface streams may feed water into the crevasse. Blue bars show the distribution of firn water infiltration rates in response to a range of pressures equivalent to that induced by a water-filled crevasse. Red bars show small stream discharge values measured in the ablation zone of Southwest Greenland. The grey shaded region shows the range of plausible discharge values estimated from the empirical relation between stream width and discharge from Smith et al. (2015), given stream widths measured from WorldView imagery in the Northwest and Southwest Greenland ice slab regions. For larger stream, water infiltrates out of the crevasse tip more slowly than water enters the crevasse opening by stream flow, suggesting that some crevasses may partially fill with water.

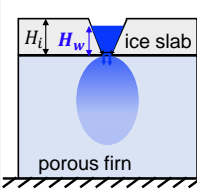
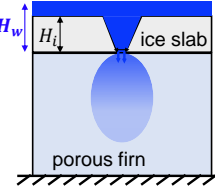
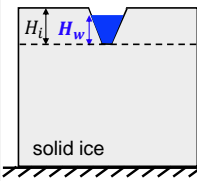
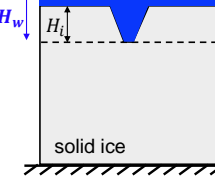
	Partially Water-Filled Crevasse ($H_w < H_i$)	Supraglacial Lake Over Crevasse ($H_w > H_i$)
Fracture in Ice Slab	 <p>Maximum Effective Stress: $\sigma'_{xx,max} = \beta b \rho_w g H_w - \frac{\nu}{1-\nu} \rho_i g H_i$</p> <p>Non-Dimensional Stress: $\bar{\sigma}'_{xx,max} = \beta b \left(\frac{\rho_w}{\rho_i}\right) \bar{H} - \frac{\nu}{1-\nu}$</p>	 <p>Maximum Effective Stress: $\sigma'_{xx,max} = \beta b \rho_w g H_w - \frac{\nu}{1-\nu} [\rho_i g H_i + \rho_w g (H_w - H_i)]$</p> <p>Non-Dimensional Stress: $\bar{\sigma}'_{xx,max} = \left(\beta b - \frac{\nu}{1-\nu}\right) \left(\frac{\rho_w}{\rho_i}\right) \bar{H} - \frac{\nu}{1-\nu} \left(1 - \frac{\rho_w}{\rho_i}\right)$</p>
Fracture in Solid Ice	 <p>Maximum Effective Stress: $\sigma'_{xx,max} = \rho_w g H_w - \rho_i g H_i$</p> <p>Non-Dimensional Stress: $\bar{\sigma}'_{xx,max} = \left(\frac{\rho_w}{\rho_i}\right) \bar{H} - 1$</p>	 <p>Maximum Effective Stress: $\sigma'_{xx,max} = \rho_w g H_w - \rho_i g H_i - \rho_w g (H_w - H_i)$</p> <p>Non-Dimensional Stress: $\bar{\sigma}'_{xx,max} = \left(\frac{\rho_w}{\rho_i}\right) - 1$</p>

Fig. 9. The theoretical prediction of the maximum effective stress at the crevasse tip $\sigma'_{xx,max}$. We present $\sigma'_{xx,max}$ in both dimensional and dimensionless forms.

314 possible that we overestimate the typical discharge for large streams, since the Smith and others (2015)
 315 empirical relation was calibrated during a particularly high melt year and in the ablation zone where melt
 316 rates are higher. However, given that our firn infiltration rates are also overestimated, since they are based
 317 on the pressure of a fully water-filled crevasse, we assess that it is still plausible that some crevasses in ice
 318 slab regions may fill with water. Therefore, we address the second question – does hydrostatic loading of
 319 an ice slab crevasse induce sufficient stress in the firn layer to initiate fracture?

320 4.3 Maximum effective stress in the firn layer

321 4.3.1 Effects of water depth

We first explore how the maximum effective stress in the firn layer changes as a function of water height in the crevasse. We consider two scenarios: a partially or fully water-filled crevasse ($0 \leq H_w \leq H_i$) and a supraglacial lake overtop a crevasse ($H_w > H_i$), where the surface area of the fracture is assumed to be negligible when compared to the total extent of the lake. Unfortunately, it is difficult to directly quantify if or when the magnitude of the maximum effective stress meets the fracture criterion defined in Eqn. 31 for two reasons. First, the tensile strength of firn (σ'_t) is not well constrained, particularly in Greenland where the mechanical properties may be significantly altered by water infiltration and refreezing. Second, we are not aware of a reliable way to estimate the background glaciological stress due to ice flow in a solid mechanics framework. This would require measurements of the background strain ($\epsilon_{xx,0}$, rather than strain

rate) at an appropriate time scale, which is not well-defined. Therefore, instead of directly comparing the total maximum effective stress in the firn to the tensile strength of firn, we instead compare the maximum effective stress in the firn to the total stress at the crevasse tip in an equivalent system composed of solid ice. In this way, we can evaluate whether the presence of firn will increase or decrease the likelihood of full-depth hydrofracture without assuming a particular value of tensile strength. To further simplify the analysis, we neglect the poorly-defined stress component due to the background glaciological strain ($\epsilon_{xx,0}$), since this term is additive and should be of a similar magnitude for both the ice slab-firn case and solid ice case. Therefore, it should have minimal impact on the relative difference between the maximum effective stress in the firn and total stress in solid ice. We then define a non-dimensional maximum effective stress and non-dimensional water height as follows and rescale Eqn. 31.

$$\tilde{\sigma}'_{xx,\max} \equiv \frac{\sigma'_{xx,\max}}{\rho_i g H_i}, \quad (35)$$

$$\tilde{H} \equiv \frac{H_w}{H_i}. \quad (36)$$

322 Figure 9 summarizes the final dimensional and non-dimensional equations for each scenario that we use in
 323 the remaining analysis, given the assumptions and simplification described above.

324 Given the equations in Figure 9, we use our Monte Carlo simulation approach to estimate the physically
 325 plausible distribution of maximum effective stresses that might be induced in the firn by a water-filled
 326 crevasse in an ice slab, given a range of water heights and the inherent uncertainty in the mechanical
 327 properties of the firn. Figure 10 shows the results of this non-dimensional analysis, with the average
 328 behavior of a ice slab-firn system shown in the white line, overlaid on a two-dimensional histogram that
 329 shows the spread of the possible solutions that would be consistent with the state of the firn in Greenland.

We find that when a firn layer is present, the maximum effective stress is always compressive, even accounting for uncertainty in the mechanical properties, and in the case of an overlying supraglacial lake, actually becomes more compressive as the lake deepens. Typically, maximum effective stress in the ice slab-firn system is less than in a solid ice system, the exception being when $\tilde{H} = \frac{H_w}{H_i} \lesssim 0.6$. The non-dimensional form of the equations provides a clear explanation for the physics underlying this behavior. We can think of the first term in each equation – some constant multiplied by \tilde{H} – as the hydrostatic term that describes how the maximum effective stress changes as the water pressure in the crevasse changes. The second term is a lithostatic term that describes the background state of stress in the system. Before water

is added to the crevasse, the maximum effective stress in the firn is greater than in solid ice, because the firn's lower Poisson ratio reduces the proportion of the overburden stress is transmitted horizontally and can act to close the fracture. However, as water begins to fill the fracture, the maximum effective stress increases more slowly in the ice slab-firn system compared to the solid ice system, because only a portion of the hydrostatic stress is transferred to the solid skeleton, with the remainder being accommodated by an increase in pore pressure. As a result, once the water level in the crevasse exceeds $H_w \gtrsim 0.6H_i$, the effective stress at the fracture tip in solid ice exceeds the maximum effective stress experienced by the firn. The exact point of this crossover can be calculated as a function of ν and b as shown in Eqn. 37.

$$\tilde{H} = \left(\frac{1 - 2\nu}{1 - \nu} \right) \left(\frac{1}{1 - \beta b} \right) \left(\frac{\rho_i}{\rho_w} \right) \approx 0.6. \quad (37)$$

330 Once $\tilde{H} \geq \frac{\rho_i}{\rho_w}$, the effective stress in the solid ice system will always be tensile. This is the critical
 331 conclusion of classical hydrofracture analyses in glaciology – that, due to the density difference between
 332 water and ice, a water-filled crevasse will always be in net tension and can propagate unstably (van der
 333 Veen, 2007; Lai and others, 2020). However, in the presence of an underlying firn layer, this transition is
 334 never reached and the maximum effective stress always remains compressive, due to the mitigating effect
 335 of pore pressure.

336 In the case of a supraglacial lake, where $H_w > H_i$, the classical solution for solid ice hydrofracture
 337 is identical to the solution for a completely water-filled crevasse and is independent of the depth of the
 338 lake. This is because the additional overburden from the lake contributes equally to the lithostatic and
 339 hydrostatic terms, so that the effective stress simply remains a function of the density difference between the
 340 ice and water in the crevasse. However, in the presence of an underlying firn layer, the maximum effective
 341 stress is significantly reduced by the presence of an overlying supraglacial lake and in fact decreases linearly
 342 as lake depth increases. The system behaves in this way because the overlying lake water contributes more
 343 to increasing the lithostatic stress acting to close the fracture than it does to increasing the hydrostatic
 344 stress, due to the competing influence of the Poisson ratio and Biot coefficient on the transfer of stress to
 345 the firn skeleton.

346 4.3.2 Effects of firn porosity

347 Since ν and b are both a function of firn porosity, we also explore the change in non-dimensional maximum
 348 effective stress as a function of firn porosity and non-dimensional water height. In Figure 11, we plot the

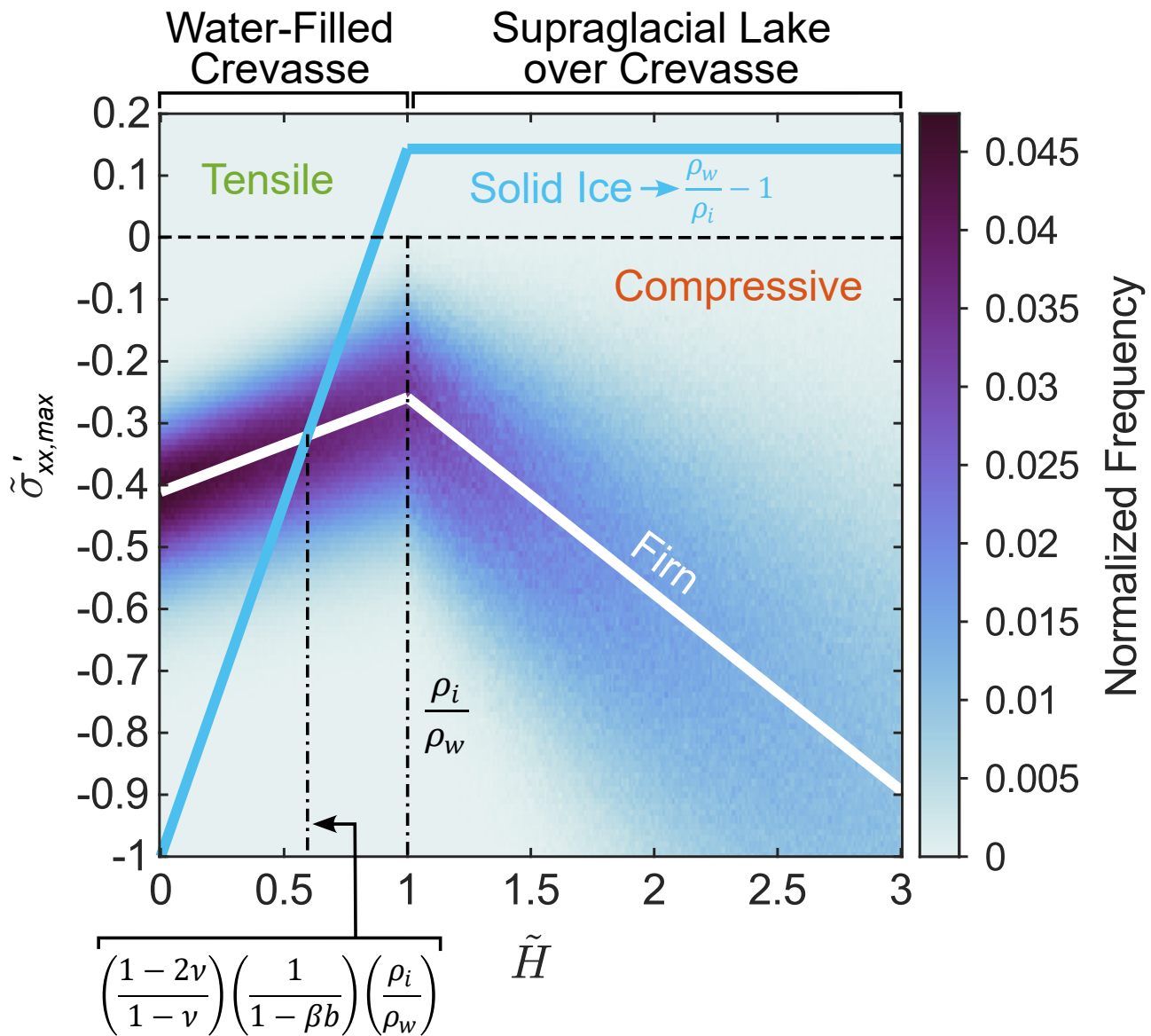


Fig. 10. Non-dimensional analysis of maximum effective stress ($\tilde{\sigma}'_{xx,max} \equiv \frac{\sigma'_{xx,max}}{\rho_i g \tilde{H}_i}$) as a function of water height within the crevasse ($\tilde{H} \equiv \frac{H_w}{H_i}$). The average behavior of an ice slab-firn system in Greenland is shown in the white line. This is overlain on a 2D histogram showing the full distribution of plausible solutions derived from the Monte Carlo analysis, given our uncertainty in the mechanical properties of the firn layer. The behavior for a solid ice system is shown in the blue line. When a firn layer is present, the maximum effective stress never becomes tensile, as most of the hydrostatic load is accommodated by a change in pore pressure, rather than being transmitted to the solid skeleton. Note that here we evaluate $\tilde{\sigma}'$ without the contribution of the background glaciological strain $\epsilon_{xx,0}$. If $\epsilon_{xx,0}$ is known it can be included via Eqn. (2).

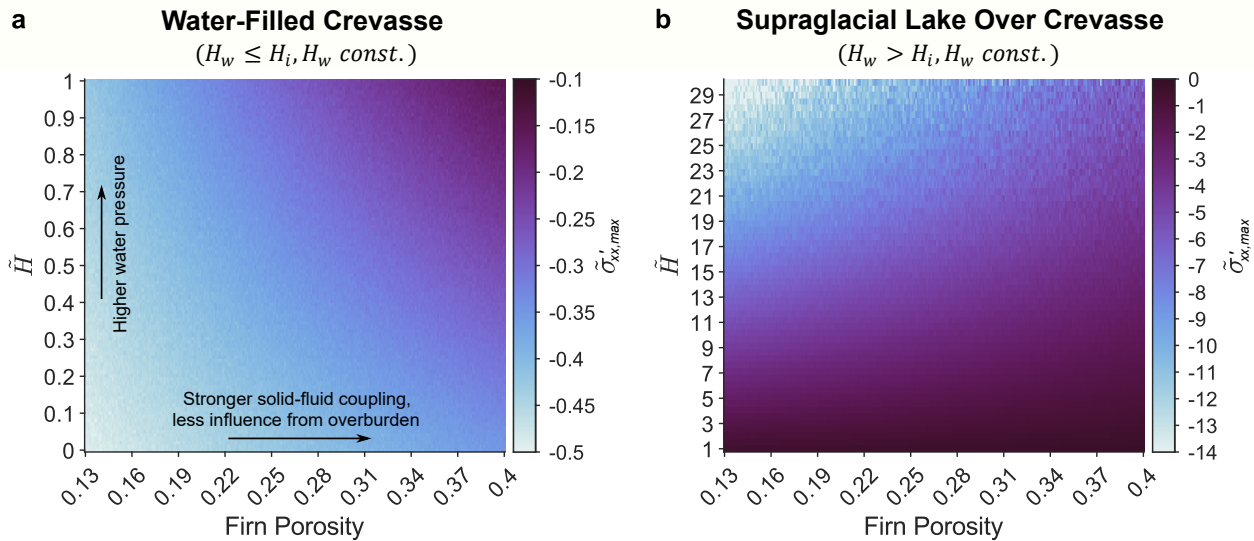


Fig. 11. Non-dimensional maximum effective stress as a function of firn porosity and non-dimensional water height in the crevasse. a) Water-filled crevasses. The non-dimensional effective stress remains compressive but increases as firn porosity increases and water height increases due to the increasing water pressure, stronger fluid-solid coupling, and reduced lithostatic stress due to a lower Poisson ratio. b) Supraglacial lake over a crevasse. Non-dimensional effective stress becomes more compressive as the water level increases, due to the additional lithostatic stress from the overlying lake. Firn porosity plays a great role in determining the non-dimensional effective stress as the water level increases, since it modulates both the hydrostatic stress transmitted to the solid skeleton, and the portion of the lithostatic stress transmitted horizontally.

349 same Monte Carlo data points shown in the histogram in Figure 10 in firn porosity versus $\tilde{H} \equiv \frac{H_w}{H_i}$ space,
350 taking the median simulation values in each 2D bin. For a partially or fully water-filled crevasse, the
351 effective stress increases as the water height increases, due to the greater hydrostatic pressure. Effective
352 stress also increases as firn porosity increases. Softer, more porous firn has a higher Biot coefficient and
353 therefore a stronger fluid-solid coupling, so more of the hydrostatic stress is felt by the solid skeleton.
354 More porous firn is also more compressible and has a lower Poisson ratio, so less of the lithostatic stress
355 is transmitted horizontally and can act to close the crevasse. Instead, the firn compacts vertically under
356 the overburden. In the case of a supraglacial lake over a crevasse, we instead find that an increase in lake
357 depth reduces the effective stress due to the increasing influence of the lithostatic stress component. As
358 expected, effective stress still increases as firn porosity increases, but this influence is more significant at
359 greater lake depths, since it reflects how the coupling between hydrostatic stress and maximum effective
360 stress is modulated by the Biot coefficient. Overall, we find that a low porosity, stiff firn matrix is the most
361 stable.

362 5. DISCUSSION

363 Our results demonstrate that the presence of a porous firn layer underneath Greenland's ice slabs leads
364 to a significant resilience to hydrofracture in these regions. Where water drains into crevasses through
365 hillslope flow or small streams, the rate of water injection into the crevasse is closely balanced by the
366 rate at which water infiltrates into the permeable firn layer. As a result, water will not rise within the
367 fracture and the hydrostatic pressure on the firn remains low and insufficient to cause hydrofracture in the
368 firn layer. Where large streams, rivers, or lakes intersect fractures, the rate of surface water inflow may be
369 significantly greater than the firn infiltration rate, leading to crevasse filling. However, even in this case,
370 the firn largely stabilizes the system and prevents hydrofracture.

371 Specifically, we find that at water levels below the critical transition point defined in Eqn. 37, the
372 underlying firn layer experiences a slightly greater maximum effective stress than if the system consisted
373 of solid ice as shown in Figure 10. However, in both cases, the effective stress remains compressive. Once
374 the water level exceeds this transition point, the firn becomes a stabilizing mechanism that significantly
375 reduces the maximum effective stress as 78% of the total stress is accommodated by a change in pore
376 pressure, rather than being transmitted to the solid skeleton. In the case of a supraglacial lake, a firn layer
377 is particularly stabilizing as the lithostatic stress increases more quickly with lake depth than the hydrostatic

378 stress. Therefore, even in the case of a fully water-filled crevasse, hydrofracture of a porous firn layer
379 appears to be highly unlikely. It is important to note that we do not include the effect of glaciological
380 stresses due to ice flow in our analysis. Therefore, while it is clear that an ice slab-firn system is less likely
381 to hydrofracture than a solid ice system under the same conditions, given sufficient background stress,
382 hydrofracture in firn would certainly also be possible. A complete analysis of the conditions under which
383 this might occur would require improved estimates of the tensile strength of icy firn, as well as a validated
384 method for measuring ice strain over the relevant time scale within this solid mechanics approach.

385 **5.1 Implications for Greenland**

386 These results are consistent with the observations of ice blob formation in the Northwest Greenland ice slab
387 region discussed in the introduction. Where a porous firn layer exists, the system is infiltration-dominated
388 and leak-off of water from the fracture into the porous firn significantly reduces the likelihood of further
389 crevasse propagation. Our analysis shows that this holds for all observed ice slab configurations on the
390 Greenland Ice Sheet, not particular to the northwest. More generally, our work quantitatively validates
391 the speculation in Culberg and others (2022) that a solid ice column is needed for hydrofracture and that
392 therefore, as Greenland warms, there will be a time lag between the development of ice slabs and the
393 formation of surface-to-bed connections that can couple the supraglacial and subglacial hydrology.

394 **5.2 Implications for Antarctica**

395 These results also have important implications for the future stability of Antarctica's ice shelves. Hy-
396 drofracture has been implicated in the breakup of the Larsen B and other ice shelves (Scambos and others,
397 2000; Banwell and others, 2013; Scambos and others, 2003), leading to a loss of buttressing and significant
398 accelerations in inland ice flow that increase mass loss from the continent (Scambos and others, 2004;
399 Rignot and others, 2004). However, most ice shelves still retain some firn layer, and previous work hypoth-
400 esized that all pore space in the firn would need to be filled with refrozen meltwater before hydrofracture
401 could occur (Alley and others, 2018; Munneke and others, 2014). This hypothesis was based on the as-
402 sumption that surface ponds could not form until the firn layer was completely removed (Munneke and
403 others, 2014). The discovery of ice slabs in Greenland has since demonstrated that supraglacial hydrol-
404 ogy may develop without complete filling of firn pore space (MacFerrin and others, 2019; Tedstone and
405 Machguth, 2022), suggesting a potential mode for more rapid destabilization of ice shelves under ongoing

406 atmospheric warming. Our results now quantitatively demonstrate that even if ice shelves were to develop
407 ice slabs and rapidly transition from firn storage to supraglacial runoff in a similar way to Greenland, this
408 alone would not be sufficient to prime them for immediate hydrofracture-induced disintegration. Instead,
409 complete filling off all local firn pore space with solid ice may be necessary because of the firn's resilience
410 to hydrofracture. This would require a longer period of sustained warming to achieve than the formation
411 of ice slabs alone.

412 5.3 Assumptions and future work

413 While we have derived an idealized description of maximum effective tensile stress in the firn under a static
414 water load, our results rest on a number of modeling assumptions that should be tested in future work.
415 For example, since capillary pressure is insufficient to drive firn deformation or fracturing, we have focused
416 on water infiltration rates that are much larger than the firn hydraulic conductivity, and thus can safely
417 neglect capillarity in the model. Therefore our model cannot capture the gravity fingering instability under
418 unsaturated flow conditions (Cueto-Felgueroso and Juanes, 2009). The effect of capillarity is beyond the
419 scope of the current study, but might be important for studying the formation of ice pipes or ice lenses.
420 With the large water infiltration rates in the model, it takes only several minutes to penetrate the depth
421 of the firn layer. Therefore we neglect meltwater refreezing that takes hours (Moure and others, 2023) and
422 snow compaction that takes years (Meyer and Hewitt, 2017).

423 The current poroelastic fracture criteria does not converge to the solid fracture criteria as the porosity
424 or permeability is reduced. The difference comes from the boundary condition at the fracture tip. For
425 solid ice, the medium is impermeable, and therefore the change of horizontal effective stress at the fracture
426 tip is equal to the hydrostatic water pressure, $\delta\sigma'_{xx}|_{x=z=0} = \rho_w g H_w$. For porous firn, we assume the firn
427 layer underneath the crevasse tip is fully permeable (even as the porosity decreases) and leaves the skeleton
428 stress-free at the crevasse tip, $\delta\sigma'_{xx}|_{x=z=0} = 0$. Such assumption aligns with the fact that the effective stress
429 always vanishes at the free surface of the solid skeleton in a porous medium (MacMinn and others, 2015;
430 Auton and MacMinn, 2019; Meng and others, 2023). To span the transition from porous and permeable firn
431 to non-porous and impermeable solid ice, we could introduce a "permeability load parameter" to modulate
432 the boundary condition, as suggested in Auton and MacMinn (2019).

433 In terms of fracture dynamics, our model only predicts the conditions needed for fracture initiation in
434 the firn layer and does not consider the dynamics of fracture propagation. Future work might consider

435 the behavior of deeper crevasses that partially penetrate the firn layer, or the full transient propagation
436 path of a shallower water-filled crevasse that initially is entirely within the ice slab. Similarly, here we
437 have considered a static water load, but a fully transient model could be used to study the effect of diurnal
438 fluctuations in water levels (or other transient filling processes) on the evolution of effective stress within
439 the firn layer. As previously discussed, future work that incorporates background stresses due to the flow
440 of ice, as well as the estimates of the tensile strength of firn, would also be of significant value.

441 **6. CONCLUSIONS**

442 Understanding the vulnerability of Greenland's ice slab regions to hydrofracture is critical for assessing
443 where and how quickly the supraglacial and subglacial hydrologic systems can become coupled as the
444 equilibrium line retreats inland. Previous observational work suggested that when meltwater drains into
445 fractures in ice slabs, the water is largely be trapped in the underlying porous firn layer and does not reach
446 the ice sheet bed (Culberg and others, 2022). However, this work presented little theoretical argument to
447 support the idea that fractures could not propagate through a firn layer. Here, we developed a porome-
448 chanical model to analyze the maximum effective stress in the firn layer beneath a water-filled fracture in
449 an ice slab. Our results show that the firn layer stabilizes the system in two ways. First, for low rates
450 of water flow into a crevasse, this water can quickly leak-off into the firn and prevent the crevasse from
451 filling in the first place. Second, even if water can fill the crevasse, a significant portion of the hydrostatic
452 stress is accommodated by changes in pore pressure, reducing the effective stress felt by the solid skeleton
453 and preventing fracture propagation in firn. Indeed, we find that the maximum effective stress in the firn
454 remains compressive for all reasonable values of the firn material and hydraulic parameters and ice slab
455 and crevasse geometries. This demonstrates that firn is broadly resilient to hydrofracture across a wide
456 range of ice sheet conditions and confirms that surface-to-bed connections are unlikely to develop until all
457 local pore space has been filled with refrozen ice, with the possible exception of regions with very high
458 background stresses due to ice flow. Our model now provides a clear quantitative backing and physical
459 explanation for the apparent lack of surface-to-bed connections in ice slab regions.

460 **ACKNOWLEDGEMENTS**

461 Y.M. and C.-Y.L. acknowledge funding from the Cooperative Institute for Modeling the Earth System
462 (CIMES) at Princeton University. R.C. thanks the Department of Geosciences at Princeton University

463 for funding through the Hess Postdoctoral Fellowship. C.-Y.L. acknowledges funding from NSF's Office of
464 Polar Programs through OPP-2235051. Geospatial support for this work provided by the Polar Geospatial
465 Center under NSF-OPP awards 1043681, 1559691, and 2129685.

466 **AUTHORS' CONTRIBUTIONS**

467 Y. Meng and R. Culberg contributed equally to this work. Y. Meng developed the poromechanical model
468 and conducted the scaling analyses, R. Culberg conceived the study and applied the model to the Greenland
469 ice sheet, and C.-Y. Lai contributed to the development of the analyses and the interpretation of results.
470 All authors contributed to the writing of the paper.

471 **REFERENCES**

- 472 Adolph AC and Albert MR (2014) Gas diffusivity and permeability through the firn column at Summit, Greenland:
473 Measurements and comparison to microstructural properties. *The Cryosphere*, **8**(1), 319–328 (doi: 10.5194/tc-8-
474 319-2014)
- 475 Alley K, Scambos T, Miller J, Long D and MacFerrin M (2018) Quantifying vulnerability of antarctic ice shelves
476 to hydrofracture using microwave scattering properties. *Remote Sensing of Environment*, **210**, 297–306 (doi:
477 10.1016/j.rse.2018.03.025)
- 478 Andrews LC, Hoffman MJ, Neumann TA, Catania GA, Lüthi MP, Hawley RL, Schild KM, Ryser C and Morriss BF
479 (2018) Seasonal evolution of the subglacial hydrologic system modified by supraglacial lake drainage in western
480 greenland. *Journal of Geophysical Research: Earth Surface*, **123**(6), 1479–1496 (doi: 10.1029/2017JF004585)
- 481 Auton LC and MacMinn CW (2019) Large poroelasto-plastic deformations due to radially outward fluid injection.
482 *Journal of the Mechanics and Physics of Solids*, **132**, 103690 (doi: 10.1016/j.jmps.2019.103690)
- 483 Banwell AF, MacAyeal DR and Sergienko OV (2013) Breakup of the Larsen B Ice Shelf triggered by chain reaction
484 drainage of supraglacial lakes. *Geophysical Research Letters*, **40**(22), 5872–5876 (doi: 10.1002/2013GL057694)
- 485 Biot MA (1941) General theory of three-dimensional consolidation. *Journal of Applied Physics*, **12**(2), 155–164 (doi:
486 10.1063/1.1712886)
- 487 Bjørnaraå TI, Nordbotten JM and Park J (2016) Vertically integrated models for coupled two-phase flow and geome-
488 chanics in porous media. *Water Resources Research*, **52**(2), 1398–1417 (doi: 10.1002/2015WR017290)
- 489 Bungler AP, Detournay E and Garagash DI (2005) Toughness-dominated hydraulic fracture with leak-off. *Interna-
490 tional Journal of Fracture*, **134**, 175–190 (doi: 10.1007/s10704-005-0154-0)

- 491 Chen B, Barboza BR, Sun Y, Bai J, Thomas HR, Dutko M, Cottrell M and Li C (2022) A review of hydraulic
492 fracturing simulation. *Archives of Computational Methods in Engineering*, **29**(4), 2113–2170 (doi: 10.1007/s11831-
493 021-09653-z)
- 494 Colosio P, Tedesco M, Ranzi R and Fettweis X (2021) Surface melting over the Greenland ice sheet derived from
495 enhanced resolution passive microwave brightness temperatures (1979-2019). *The Cryosphere*, **15**(6), 2623–2646
496 (doi: 10.5194/tc-15-2623-2021)
- 497 Coussy O (2004) *Poromechanics*. John Wiley and Sons, Chichester, England, ISBN 9780470092712 (doi:
498 10.1002/0470092718)
- 499 Cueto-Felgueroso L and Juanes R (2009) A phase field model of unsaturated flow. *Water Resources Research*, **45**(10),
500 W10409 (doi: 10.1029/2009WR007945)
- 501 Culberg R, Chu W and Schroeder DM (2022) Shallow fracture buffers high elevation runoff in Northwest Greenland.
502 *Geophysical Research Letters*, **49**(23), e2022GL101151 (doi: 10.1029/2022GL101151)
- 503 Das SB, Joughin I, Behn MD, Howat IM, King MA, Lizarralde D and Bhatia MP (2008) Fracture propagation to the
504 base of the greenland ice sheet during supraglacial lake drainage. *Science*, **320**(5877), 778–781 (doi: 10.1126/sci-
505 ence.1153360)
- 506 Detournay E (2016) Mechanics of hydraulic fractures. *Annual Review of Fluid Mechanics*, **48**, 311–339 (doi:
507 10.1146/annurev-fluid-010814-014736)
- 508 Dow CF, Kulesa B, Rutt I, Tsai V, Pimentel S, Doyle S, Van As D, Lindbäck K, Pettersson R, Jones G and
509 others (2015) Modeling of subglacial hydrological development following rapid supraglacial lake drainage. *Journal*
510 *of Geophysical Research: Earth Surface*, **120**(6), 1127–1147 (doi: 10.1002/2014JF003333)
- 511 Fettweis X, Tedesco M, Van Den Broeke M and Ettema J (2011) Melting trends over the Greenland ice sheet
512 (1958-2009) from spaceborne microwave data and regional climate models. *The Cryosphere*, **5**(2), 359–375 (doi:
513 10.5194/tc-5-359-2011)
- 514 Forster RR, Box JE, Van Den Broeke MR, Miège C, Burgess EW, Van Angelen JH, Lenaerts JT, Koenig LS, Paden
515 J, Lewis C, Gogineni SP, Leuschen C, McConnell JR, Miegé C, Burgess EW, Van Angelen JH, Lenaerts JT, Koenig
516 LS, Paden J, Lewis C, Gogineni SP, Leuschen C and McConnell JR (2014) Extensive liquid meltwater storage in
517 firn within the Greenland ice sheet. *Nature Geoscience*, **7**(2), 95–98 (doi: 10.1038/ngeo2043)
- 518 Gleason CJ, Smith LC, Chu VW, Legleiter CJ, Pitcher LH, Overstreet BT, Rennermalm AK, Forster RR and
519 Yang K (2016) Characterizing supraglacial meltwater channel hydraulics on the Greenland Ice Sheet from in situ
520 observations. *Earth Surface Processes and Landforms*, **41**(14), 2111–2122 (doi: 10.1002/esp.3977)

- 521 Haimson B and Fairhurst C (1969) Hydraulic fracturing in porous-permeable materials. *Journal of Petroleum Tech-*
522 *nology*, **21**(07), 811–817 (doi: 10.2118/2354-PA)
- 523 Harper J, Humphrey N, Pfeffer WT, Brown J and Fettweis X (2012) Greenland ice-sheet contribution to sea-level
524 rise buffered by meltwater storage in firn. *Nature*, **491**(7423), 240–243 (doi: 10.1038/nature11566)
- 525 Hoffman MJ, Perego M, Andrews LC, Price SF, Neumann TA, Johnson JV, Catania G and Lüthi MP (2018)
526 Widespread moulin formation during supraglacial lake drainages in greenland. *Geophysical Research Letters*, **45**(2),
527 778–788 (doi: 10.1002/2017GL075659)
- 528 Jha B and Juanes R (2014) Coupled multiphase flow and poromechanics: A computational model of pore
529 pressure effects on fault slip and earthquake triggering. *Water Resources Research*, **50**(5), 3776–3808 (doi:
530 10.1002/2013WR015175)
- 531 King EC and Jarvis EP (2007) Use of shear waves to measure poisson’s ratio in polar firn. *Journal of Environmental*
532 *and Engineering Geophysics*, **12**(1), 15–21 (doi: 10.2113/JEEG12.1.15)
- 533 Koziol C, Arnold N, Pope A and Colgan W (2017) Quantifying supraglacial meltwater pathways in the Paakitsoq
534 region, West Greenland. *Journal of Glaciology*, **63**(239), 464–476 (doi: 10.1017/jog.2017.5)
- 535 Lai CY, Kingslake J, Wearing MG, Chen PHC, Gentine P, Li H, Spergel JJ and van Wessem JM (2020) Vulnerability
536 of Antarctica’s ice shelves to meltwater-driven fracture. *Nature*, **584**(7822), 574–578 (doi: 10.1038/s41586-020-
537 2627-8)
- 538 Lai CY, Stevens LA, Chase DL, Creyts TT, Behn MD, Das SB and Stone HA (2021) Hydraulic transmissivity
539 inferred from ice-sheet relaxation following greenland supraglacial lake drainages. *Nature Communications*, **12**(1),
540 3955 (doi: 10.1038/s41467-021-24186-6)
- 541 Lewis RW and Schrefler BA (1999) *The finite element method in the static and dynamic deformation and consolidation*
542 *of porous media*. John Wiley & Sons, Chichester, England, ISBN 978-0-471-92809-6
- 543 MacFerrin MJ, Machguth H, As Dv, Charalampidis C, Stevens CM, Heilig A, Vandecrux B, Langen PL, Mottram
544 R, Fettweis X and others (2019) Rapid expansion of Greenland’s low-permeability ice slabs. *Nature*, **573**(7774),
545 403–407 (doi: 10.1038/s41586-019-1550-3)
- 546 MacFerrin MJ, Stevens CM, Vandecrux B, Waddington ED and Abdalati W (2022) The Greenland firn compaction
547 verification and reconnaissance (FirnCover) dataset, 2013-2019. *Earth System Science Data*, **14**(2), 955–971 (doi:
548 10.5194/essd-14-955-2022)

- 549 Machguth H, Macferrin M, Van As D, Box JE, Charalampidis C, Colgan W, Fausto RS, Meijer HA, Mosley-Thompson
550 E and Van De Wal RS (2016) Greenland meltwater storage in firn limited by near-surface ice formation. *Nature*
551 *Climate Change*, **6**(4), 390–393 (doi: 10.1038/nclimate2899)
- 552 MacMinn CW, Dufresne ER and Wettlaufer JS (2015) Fluid-driven deformation of a soft granular material. *Physical*
553 *Review X*, **5**(1), 011020 (doi: 10.1103/PhysRevX.5.011020)
- 554 Meng Y, Primkulov BK, Yang Z, Kwok CY and Juanes R (2020) Jamming transition and emergence of fracturing
555 in wet granular media. *Physical Review Research*, **2**(2), 022012 (doi: 10.1103/PhysRevResearch.2.022012)
- 556 Meng Y, Li W and Juanes R (2022) Fracturing in wet granular media illuminated by photoporomechanics. *Physical*
557 *Review Applied*, **18**(6), 064081 (doi: 10.1103/PhysRevApplied.18.064081)
- 558 Meng Y, Li W and Juanes R (2023) Crossover from viscous fingering to fracturing in cohesive wet granular media:
559 a photoporomechanics study. *Soft Matter*, **19**(37), 7136–7148 (doi: 10.1039/D3SM00897E)
- 560 Meyer CR and Hewitt IJ (2017) A continuum model for meltwater flow through compacting snow. *The Cryosphere*,
561 **11**(6), 2799–2813 (doi: 10.5194/tc-11-2799-2017)
- 562 Moon T, Joughin I, Smith B, Van Den Broeke MR, Van De Berg WJ, Noël B and Usher M (2014) Distinct patterns of
563 seasonal Greenland glacier velocity. *Geophysical Research Letters*, **41**(20), 7209–7216 (doi: 10.1002/2014GL061836)
- 564 Mouginot J, Rignot E, Bjørk AA, van den Broeke M, Millan R, Morlighem M, Noël B, Scheuchl B and Wood M
565 (2019) Forty-six years of Greenland Ice Sheet mass balance from 1972 to 2018. *Proceedings of the National Academy*
566 *of Sciences of the United States of America*, **116**(19), 9239–9244 (doi: 10.1073/pnas.1904242116)
- 567 Moure A, Jones N, Pawlak J, Meyer C and Fu X (2023) A thermodynamic nonequilibrium model for pref-
568 erential infiltration and refreezing of melt in snow. *Water Resources Research*, **59**(5), e2022WR034035 (doi:
569 10.1029/2022WR034035)
- 570 Munneke PK, Ligtenberg SR, Van Den Broeke MR and Vaughan DG (2014) Firn air depletion as a precursor of
571 antarctic ice-shelf collapse. *Journal of Glaciology*, **60**(220), 205–214 (doi: 10.3189/2014JoG13J183)
- 572 Petrovic J (2003) Review mechanical properties of ice and snow. *Journal of Materials Science*, **38**, 1–6 (doi:
573 10.1023/A:1021134128038)
- 574 Poinar K and Andrews LC (2021) Challenges in predicting greenland supraglacial lake drainages at the regional scale.
575 *The Cryosphere*, **15**(3), 1455–1483 (doi: 10.5194/tc-15-1455-2021)
- 576 Poinar K, Joughin I, Lilien D, Brucker L, Kehrl L and Nowicki S (2017) Drainage of southeast greenland firn aquifer
577 water through crevasses to the bed. *Frontiers in Earth Science*, **5**(5), 10–3389 (doi: 10.3389/feart.2017.00005)

- 578 Rignot E, Casassa G, Gogineni P, Krabill W, Rivera A and Thomas R (2004) Accelerated ice discharge from the
579 Antarctic Peninsula following the collapse of Larsen B ice shelf. *Geophysical Research Letters*, **31**(18), L18401 (doi:
580 10.1029/2004GL020697)
- 581 Sayers CM (2021) Porosity dependence of elastic moduli of snow and firn. *Journal of Glaciology*, **67**(265), 788–796
582 (doi: 10.1017/jog.2021.25)
- 583 Scambos T, Hulbe C and Fahnestock M (2003) Climate-induced ice shelf disintegration in the antarctic penin-
584 sula. *Antarctic Peninsula Climate Variability: Historical and Paleoenvironmental Perspectives*, **79**, 79–92 (doi:
585 10.1029/AR079p0079)
- 586 Scambos TA, Hulbe C, Fahnestock M and Bohlander J (2000) The link between climate warming and break-up of ice
587 shelves in the antarctic peninsula. *Journal of Glaciology*, **46**(154), 516–530 (doi: 10.3189/172756500781833043)
- 588 Scambos TA, Bohlander J, Shuman CA and Skvarca P (2004) Glacier acceleration and thinning after ice shelf collapse
589 in the larsen b embayment, antarctica. *Geophysical Research Letters*, **31**(18), L18402 (doi: 10.1029/2004GL020670)
- 590 Schlegel R, Diez A, Löwe H, Mayer C, Lambrecht A, Freitag J, Miller H, Hofstede C and Eisen O (2019) Comparison
591 of elastic moduli from seismic diving-wave and ice-core microstructure analysis in Antarctic polar firn. *Annals of*
592 *Glaciology*, **60**(79), 220–230 (doi: 10.1017/aog.2019.10)
- 593 Schoof C (2010) Ice-sheet acceleration driven by melt supply variability. *Nature*, **468**(7325), 803–806 (doi: 10.1038/na-
594 ture09618)
- 595 Shimaki Y and Arakawa M (2021) Tensile strength and elastic properties of fine-grained ice aggregates: Implications
596 for crater formation on small icy bodies. *Icarus*, **369**, 114646 (doi: 10.1016/j.icarus.2021.114646)
- 597 Smith JL (1965) *The elastic constants, strength and density of Greenland snow as determined from measurements of*
598 *sonic wave velocity*, volume 167. US Army Cold Regions Research & Engineering Laboratory
- 599 Smith LC, Chu VW, Yang K, Gleason CJ, Pitcher LH, Rennermalm AK, Legleiter CJ, Behar AE, Overstreet BT,
600 Moustafa SE, Tedesco M, Forster RR, LeWinter AL, Finnegan DC, Sheng Y and Balog J (2015) Efficient meltwater
601 drainage through supraglacial streams and rivers on the southwest Greenland ice sheet. *Proceedings of the National*
602 *Academy of Sciences of the United States of America*, **112**(4), 1001–1006 (doi: 10.1073/pnas.1413024112)
- 603 Stevens LA, Behn MD, McGuire JJ, Das SB, Joughin I, Herring T, Shean DE and King MA (2015) Green-
604 land supraglacial lake drainages triggered by hydrologically induced basal slip. *Nature*, **522**(7554), 73–76 (doi:
605 10.1038/nature14480)
- 606 Tedstone AJ and Machguth H (2022) Increasing surface runoff from Greenland's firn areas. *Nature Climate Change*,
607 **12**(7), 672–676 (doi: 10.1038/s41558-022-01371-z)

- 608 Terzaghi K (1943) *Theoretical soil mechanics*. John Wiley & Sons, Ltd, New York, USA, ISBN 9780470172766 (doi:
609 10.1002/9780470172766)
- 610 Van Den Broeke M, Bamber J, Ettema J, Rignot E, Schrama E, Van Berg WJD, Van Meijgaard E, Velicogna I
611 and Wouters B (2009) Partitioning recent Greenland mass loss. *Science*, **326**(5955), 984–986 (doi: 10.1126/sci-
612 ence.1178176)
- 613 van der Veen CJ (2007) Fracture propagation as means of rapidly transferring surface meltwater to the base of
614 glaciers. *Geophysical Research Letters*, **34**(1), L01501 (doi: 10.1029/2006GL028385)
- 615 Wang HF (2000) *Theory of linear poroelasticity with applications to geomechanics and hydrogeology*. Princeton Uni-
616 versity Press, New Jersey, USA, ISBN 9780691037462 (doi: 10.1515/9781400885688)
- 617 Yang K and Smith LC (2016) Internally drained catchments dominate supraglacial hydrology of the southwest Green-
618 land Ice Sheet. *Journal of Geophysical Research: Earth Surface*, **121**(10), 1891–1910 (doi: 10.1002/2016JF003927)
- 619 Zwally HJ, Abdalati W, Herring T, Larson K, Saba J and Steffen K (2002) Surface melt-induced acceleration of
620 Greenland ice-sheet flow. *Science*, **297**(5579), 218–222 (doi: 10.1126/science.1072708)